

## Mapping the zonal structure of Titan's northern polar vortex

Jason Sharkey<sup>a,\*</sup>, Nicholas A. Teanby<sup>a</sup>, Melody Sylvestre<sup>a</sup>, Dann M. Mitchell<sup>b</sup>, William J. M. Seviour<sup>b</sup>, Conor A. Nixon<sup>c</sup>, Patrick G.J. Irwin<sup>d</sup>

<sup>a</sup> School of Earth Sciences, University of Bristol, Wills Memorial Building, Queens Road, Bristol BS8 1RJ, UK

<sup>b</sup> School of Geographical Sciences, University of Bristol, Bristol BS8 1RL, UK

<sup>c</sup> Planetary Systems Laboratory, NASA Goddard Space Flight Center, Greenbelt, MD 20771, USA

<sup>d</sup> Atmospheric, Oceanic, & Planetary Physics, Department of Physics, University of Oxford, Clarendon Laboratory, Parks Road, Oxford OX1 3PU, UK

### ABSTRACT

Saturn exhibits an obliquity of  $26.7^\circ$  such that the largest moon, Titan, experiences seasonal variations including the formation of a polar vortex in the winter hemisphere. Titan's polar vortex is characterised by cold stratospheric temperatures due to the lack of insolation over the winter pole, and an increase in trace gas abundance as a result of complex organic chemistry in the upper atmosphere combined with polar subsidence. Meridional variations in temperature and gas abundance across the vortex have previously been investigated, but there has not yet been any in-depth study of the zonal variations in the temperature or composition of the northern vortex. Here we present the first comprehensive two-dimensional seasonal mapping of Titan's northern winter vortex. Using 18 nadir mapping sequences observed by the Composite InfraRed Spectrometer (CIRS) instrument on-board Cassini, we investigate the evolution of the vortex over almost half a Titan year, from late winter through to mid summer ( $L_s = 326 - 86^\circ$ , 2007–2017). We find the stratospheric symmetry axis to be tilted from the solid body rotation axis by around  $3.5^\circ$ , although our results for the azimuthal orientation of the tilt are inconclusive. We find that the northern vortex appears to remain zonally uniform in both temperature and composition at all times. A comparison with vortices observed on Earth, Mars, and Venus shows that large-scale wave mechanisms that are important on other terrestrial planets are not as significant in Titan's atmosphere. This allows the northern vortex to be more symmetrical and persist longer throughout the annual cycle compared to other terrestrial planets.

### 1. Introduction

Titan is the largest moon of Saturn and is host to a thick, nitrogen dominated atmosphere (around 98%) with methane the second most abundant gas, at around 1.48% in the stratosphere, and with a surface pressure of approximately 1500 mbar (Fulchignoni et al., 2005). Titan's rotation is tidally locked to Saturn, such that the length of a Titan day is the length of time taken to complete one orbit – 15.9 Earth days. Furthermore, Saturn exhibits an obliquity of  $26.7^\circ$  meaning that Titan, which orbits in Saturn's equatorial plane, experiences seasonal variations over a Titan year – 29.5 Earth years.

In Titan's upper atmosphere, nitrogen and methane molecules undergo photolysis by interaction with UV photons and magnetospheric electrons to produce free radicals which can go on to recombine with one another to create various complex hydrocarbon ( $C_xH_y$ ) and nitrile ( $H_xC_yN_z$ ) compounds (Krasnopolsky, 2009; Lavvas et al., 2008; Vuitton et al., 2019; Wilson and Atreya, 2004). These gases subside over the cold winter pole where they are shielded from UV photons, resulting in an increased trace gas abundance in the vortex. They also have a wide range of photochemical lifetimes, allowing their use as chemical probes

of different atmospheric dynamics in the vortex (Teanby et al., 2008a).

Titan General Circulation Models (GCMs) attempt to replicate the circulation of Titan's atmosphere. We do not yet have year round observations of Titan and so GCMs provide us with an opportunity to investigate how the atmosphere may behave over longer time periods than we have observed. Such models predict a relatively simple pole to pole meridional circulation, with an upwelling of gas in the summer hemisphere, which subsides over the winter pole. The circulation is expected to reverse as each hemisphere moves from summer into winter and vice versa. A brief two cell system around equinox which sees gas rising from the equator and subsiding at the poles is predicted between the transition (Hourdin et al., 1995; Lebonnois et al., 2012; Newman et al., 2011). Such models are in broad agreement with observations of trace gas enrichment in the polar vortex (Teanby et al., 2012; Vinatier et al., 2015). Titan's entire stratosphere is also tilted, such that the stratospheric rotation axis is offset from the solid body rotation axis by around  $4^\circ$  (Achterberg et al., 2008). The exact mechanism responsible for this feature is not yet fully understood. However, an early CIRS analysis of polar temperatures identified the offset and suggested that it is the result of the atmospheric spin adjusting itself to the angular

\* Corresponding author.

E-mail address: [js17419@bristol.ac.uk](mailto:js17419@bristol.ac.uk) (J. Sharkey).

<https://doi.org/10.1016/j.icarus.2019.113441>

Received 28 June 2019; Received in revised form 28 August 2019; Accepted 10 September 2019

Available online 5 October 2019

0019-1035/© 2019 Elsevier Inc. All rights reserved.

momentum transfer from solar heating (Achterberg et al., 2008). Further studies found similar results using haze albedo, composition and zonal wind velocity measurements (Roman et al., 2009; Teanby et al., 2010; West et al., 2016).

The Cassini spacecraft toured the Saturnian system from 2004 through to 2017, performing 127 targeted fly-bys of Titan over this time period, providing almost half a Titan year of observations (Nixon et al., 2019). Titan's northern spring equinox occurred in August 2009, meaning Cassini observes seasonal changes on Titan as northern winter evolves into northern summer. Many trace gases in Titan's atmosphere are found to be very IR-active and so by using IR spectra recorded by the Composite InfraRed Spectrometer (CIRS) on-board Cassini, information about the temperature and composition of Titan's atmosphere can be derived (Teanby et al., 2019).

Previous CIRS based studies of Titan's northern vortex have used both limb and nadir observations. Limb data recorded by CIRS does not provide sufficient coverage to investigate zonal variations, and most nadir studies have taken zonally averaged measurements to investigate meridional variations. These studies have shown evidence of strong latitudinal gradients in both temperature (Achterberg et al., 2008; Sylvestre et al., 2019; Teanby et al., 2019; Vinatier et al., 2015) and composition (Sylvestre et al., 2018; Teanby et al., 2008a) towards the pole in the winter hemisphere and evidence of varying gas abundance-altitude gradients depending on the season, latitude and the photochemical lifetime of the gas (Coustenis et al., 2016; Teanby et al., 2017, 2006, 2012; Vinatier et al., 2015, 2010).

Cassini provides us with a unique opportunity to study the breakup of Titan's northern polar vortex. Comparing the differences and similarities between polar vortices on other planets may provide a useful insight into the mechanisms driving their evolution. For example, the polar vortices of Earth and Mars are both observed to become highly distorted over their lifetime (Mitchell et al., 2015; Waugh and Randel, 1999; Waugh et al., 2016) with the generation of Sudden Stratospheric Warmings (SSWs) facilitating the rapid breakdown of the vortex (termed the final warming) depending on their timing in winter. Flasar and Achterberg (2009) present a comparison between the vortices of Titan and Earth. The polar vortex on Venus also displays a highly asymmetric distribution, with the formation of a so-called "vortex dipole" or 'S' shaped center (Taylor et al., 1979). However, Venus' rotation axis is almost perpendicular to its orbital plane and so the vortex formation is not seasonal, but more likely driven by internal dynamical processes (Flasar and Achterberg, 2009).

Whilst a few early Titan CIRS observations have been investigated for zonal temperature (Achterberg et al., 2008) and composition (Teanby et al., 2008a) variations, there has not yet been an extensive study of the zonal structure in Titan's temperature and trace gas abundances over the entire Cassini mission.

In this paper we present two analyses: (i) a new method to determine the magnitude and orientation of Titan's stratospheric tilt using only Cassini-CIRS trace gas emissions and (ii) a study of the zonal variations of the temperature and composition of Titan's northern polar vortex throughout the Cassini mission, from northern midwinter through to northern midsummer.

## 2. CIRS observations

CIRS is a remote sensing Fourier transform spectrometer onboard the Cassini spacecraft, measuring thermal emissions from the IR spectrum in the range  $10\text{--}1500\text{ cm}^{-1}$  ( $1\text{ mm--}7\text{ }\mu\text{m}$ ) (Flasar et al., 2004; Jennings et al., 2017). Many of the complex gas species found in Titan's atmosphere exhibit strong emission features in this wavenumber range, providing the opportunity to retrieve atmospheric temperature and composition from IR spectra. CIRS covers this range by use of two interferometers occupying a common scanning mechanism and telescope. The far-IR part of the spectrum ( $10\text{--}600\text{ cm}^{-1}$ ) is measured by a polarising interferometer (FP1), whilst the mid-IR part of the spectrum is

measured by a Michelson interferometer split across two focal planes (FP3:  $600\text{--}1100\text{ cm}^{-1}$ , FP4:  $1100\text{--}1500\text{ cm}^{-1}$ ). The instrument has an apodized spectral resolution which can be adjusted from  $0.5$  to  $15.5\text{ cm}^{-1}$ . For the purpose of this study we will use mid-IR measurements (FP3, FP4) with a spectral resolution of  $2.5\text{ cm}^{-1}$ , as these focal planes have better spatial resolution than FP1, and the wavenumber range covers both the  $\nu_4$   $\text{CH}_4$  band ( $1240\text{--}1360\text{ cm}^{-1}$ ) in FP4 and a variety of trace gas emissions in FP3. A resolution of  $2.5\text{ cm}^{-1}$  is sufficiently fine to resolve individual gas peaks and can be acquired fast enough to allow mapping observations which are ideal for studying zonal structure. Depending on season and latitude, these observations will probe pressure levels from around 10 mbar up to 0.01 mbar, with contribution functions typically peaking between 1 and 0.1 mbar.

In selecting our observations we place a few constraints. In order to study the pole, we require that the data includes measurements extending up to at least  $85^\circ\text{N}$ . Our observations must also provide substantial spatial coverage around the polar region in order to measure zonal variations. To meet this criteria, the observations selected have an average FOV span in FP3 and FP4 of around  $2.5^\circ$  of latitude at sub-spacecraft point. In each observation, CIRS typically measures around 4000 individual spectra in each of the FP3 and FP4 focal planes.

As the emission angle of an observation increases, so too does the path length through the atmosphere, leading to an artificial increase in the observed IR emissions, or "limb brightening". To minimise the effect of limb brightening around our polar data, we reject observations with a sub-spacecraft-latitude less than  $40^\circ\text{N}$ . This ensures a maximum emission angle of  $50^\circ$  at the pole.

Nixon et al. (2019) summarise the CIRS coverage of Titan over the Cassini mission. Applying our criteria we have 18 observations available for this study, ranging from early 2007 through to late 2016 (late northern winter through mid northern summer on Titan). These observations are not evenly distributed in time, with the largest gap between observations being around 4 years, from May 2009 to April 2013 – equivalent to around 0.14 Titan years. Due to the sparse temporal coverage, we are unlikely to be able to track the progression of individual features (if present) between observations, however we can treat each observation as a snapshot of Titan's atmosphere at the given time and identify any asymmetry or zonal structure present in the vortex. The selection criteria are illustrated in Fig. 1 and the selected observations are listed in Table 1.

To improve the signal-to-noise ratio of the data, the observations are calibrated using the DS4000 (version 4.2) calibration, which more effectively removes the instrument and sky background contributions than the standard calibration (Jennings et al., 2017). A binning technique was also performed whereby a tessellation of Titan's surface into equal area hexagonal bins allows spectra recorded within each bin to be averaged. This method is performed for each observation as this helps to improve the signal to noise ratio of data in bins distributed evenly across the surface, with the relatively small bin size (approximately  $1.5^\circ$ ) and nearly stationary subspacecraft point ensuring that only spectra recorded at similar emission angles are grouped together in each observation (Teanby et al., 2006).

## 3. Analysis

### 3.1. Stratospheric tilt correction

As previously discussed, Titan's middle atmosphere is offset from the geographic pole by about  $4^\circ$ . Before investigating the zonal symmetry in the vortex, we must remove the effect of the tilt of the entire atmospheric circulation. We present here a new method to determine the magnitude and orientation of the atmospheric tilt using only IR emissions of vortex enriched trace gas species. Using IR emissions instead of properties derived from retrieval calculations means we can minimise the effects of retrieval bias and also directly account for the effect of emission angle. For this analysis, three gas emission peaks were used:  $628\text{ cm}^{-1}$  ( $\text{C}_4\text{H}_2$ ),

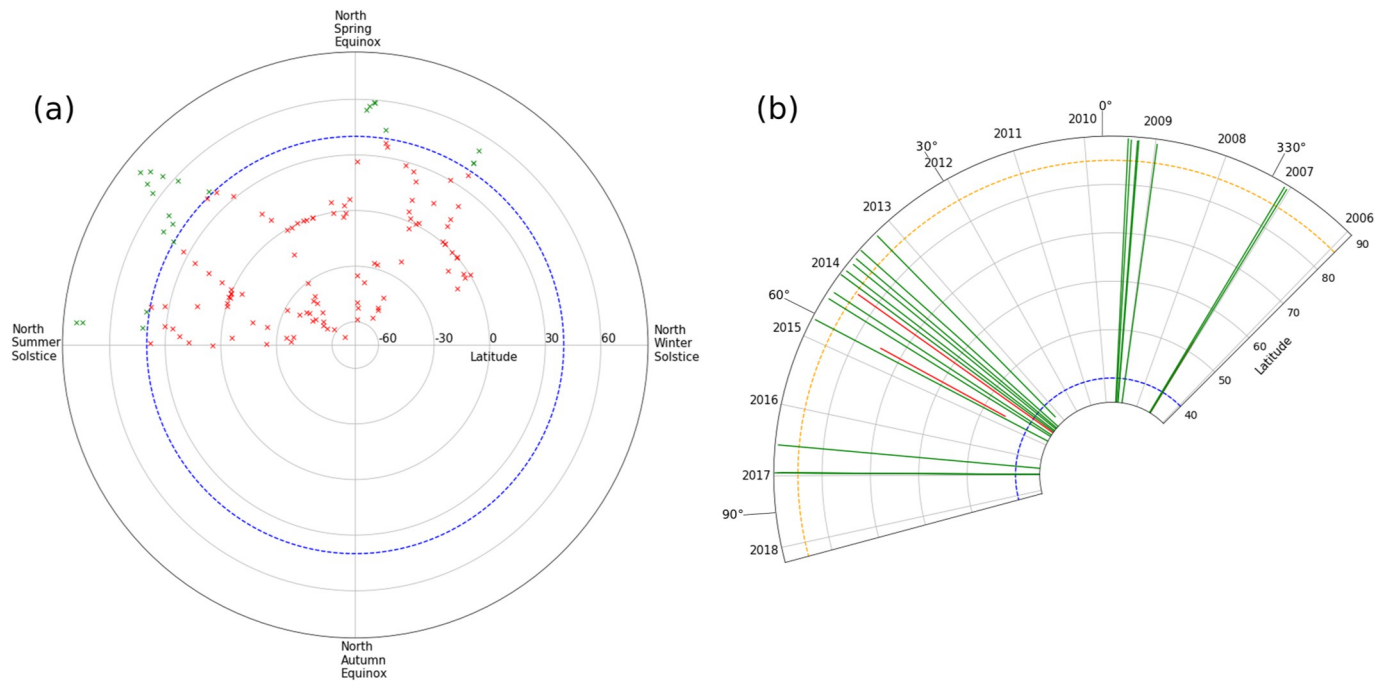


**Fig. 1.** CIRS data available for this study. (a): Seasonal coverage by CIRS is roughly half a Titan year. Markers indicate sub spacecraft latitude for each observation. Blue dashed line indicates the 40° sub spacecraft latitude criterion. Green markers indicate sub spacecraft latitude is greater than criterion. Red markers indicate sub spacecraft latitude is less than criterion. (b): Calendar year coverage and maximum latitudinal extent of each observation meeting criterion from (a), with solar longitude marked in 30° intervals. Orange dashed line indicates the 85°N coverage criterion. Green lines show latitudinal coverage of observations which meet criterion. Red lines show coverage of observations which do not meet criterion. (For interpretation of the references to color in this figure legend, the reader is referred to the web version of this article.)

**Table 1**

CIRS Observations used in this study.  $L_s$  is the solar longitude, Latitude is the sub spacecraft latitude. N indicates number of spectra measured in observation and FOV is the average field of view span at subspacecraft point.

CIRS Observation	Date	$L_s$ (°)	Latitude (° N)	FP4 N	FP3 N	FP4 FOV (°)	FP3 FOV (°)
CIRS_037TI_MIDIRTMAP002_PRIME	12/01/2007	326.95	44.6	1936	1960	2.14	2.14
CIRS_038TI_MIDIRTMAP001_PRIME	28/01/2007	327.51	51.5	1902	2132	2.50	2.50
CIRS_098TI_MIDIRTMAP002_PRIME	22/12/2008	352.04	44.6	2864	2863	2.42	2.42
CIRS_107TI_MIDIRTMAP002_PRIME	28/03/2009	355.35	58.7	4098	4092	2.54	2.54
CIRS_107TI_MIDIRTMAP001_PRIME	03/04/2009	355.56	58.4	2490	2382	2.04	2.10
CIRS_110TI_MIDIRTMAP001_PRIME	05/01/2009	356.66	56.5	4180	4183	1.88	1.88
CIRS_185TI_MIDIRTMAP001_PRIME	05/04/2013	43.76	41.9	1678	1435	2.16	2.24
CIRS_195TI_MIDIRTMAP001_PRIME	25/07/2013	47.28	57.8	7124	7134	2.68	2.69
CIRS_197TI_MIDIRTMAP001_PRIME	11/09/2013	48.78	65.8	3749	3800	2.60	2.61
CIRS_198TI_MIDIRTMAP001_PRIME	13/10/2013	49.78	72.6	7419	7382	2.63	2.62
CIRS_199TI_MIDIRTMAP001_PRIME	30/11/2013	51.27	76.4	2276	2280	2.46	2.45
CIRS_200TI_MIDIRTMAP001_PRIME	01/01/2014	52.27	69.7	4816	4792	2.41	2.41
CIRS_203TI_MIDIRTMAP001_PRIME	06/04/2014	55.25	50.0	3283	3301	2.19	2.18
CIRS_204TI_MIDIRTMAP002_PRIME	18/05/2014	56.53	45.7	2732	2728	2.11	2.11
CIRS_238TI_MIDIRTMAP002_PRIME	25/07/2016	80.99	41.4	5263	5287	2.20	2.19
CIRS_253TI_MIDIRTMAP001_PRIME	14/12/2016	85.29	42.9	4373	4417	2.84	2.84
CIRS_253TI_MIDIRTMAP002_PRIME	14/12/2016	85.31	75.3	3063	3105	2.61	2.61
CIRS_253TI_MIDIRTMAP004_PRIME	14/12/2016	85.33	78.3	1780	1779	2.92	2.92

$634\text{ cm}^{-1}(\text{C}_3\text{H}_4)$ ,  $663\text{ cm}^{-1}(\text{HC}_3\text{N})$  as the IR emission of these wave-numbers exhibit a greater radiance in the polar region compared to more equatorial latitudes as seen in Fig. 2. Fig. 2 shows maps of trace gas emissions displaying significant variation over the north pole throughout the lifetime of the Cassini mission, with greatly reduced emissions by the end of the mission indicating an increase in mixing across the vortex, likely caused by its weakening.

This polar enhancement is expected as Titan GCMs predict maximum subsidence to occur over the pole, increasing the gas abundance in this region. From these models, we expect that the temperature and composition should be broadly uniform around the vortex and so the IR emissions of trace gases should be symmetric around the vortex.

We attempt to find the center of the distribution of the chosen gas emissions, and therefore the position of the tilt, by using a minimum  $\chi^2$  method. We grid search over possible offset positions in the range  $80^\circ\text{N}$  to  $90^\circ\text{N}$  and  $0^\circ\text{W}$  to  $360^\circ\text{W}$  with  $0.1^\circ$  spacing in each direction.

As discussed earlier, large emission angles can cause observed radiances to be artificially enhanced. This is purely an effect of the geometry of the observation, and must be taken into consideration when comparing emission values. We expect that the influence of limb brightening on radiance measured at similar emission angles will be comparable. Therefore, to remove any dependence on emission angle we must only compare radiances measured at the same emission angle. To simplify this method, we rotate the data into a frame centered around



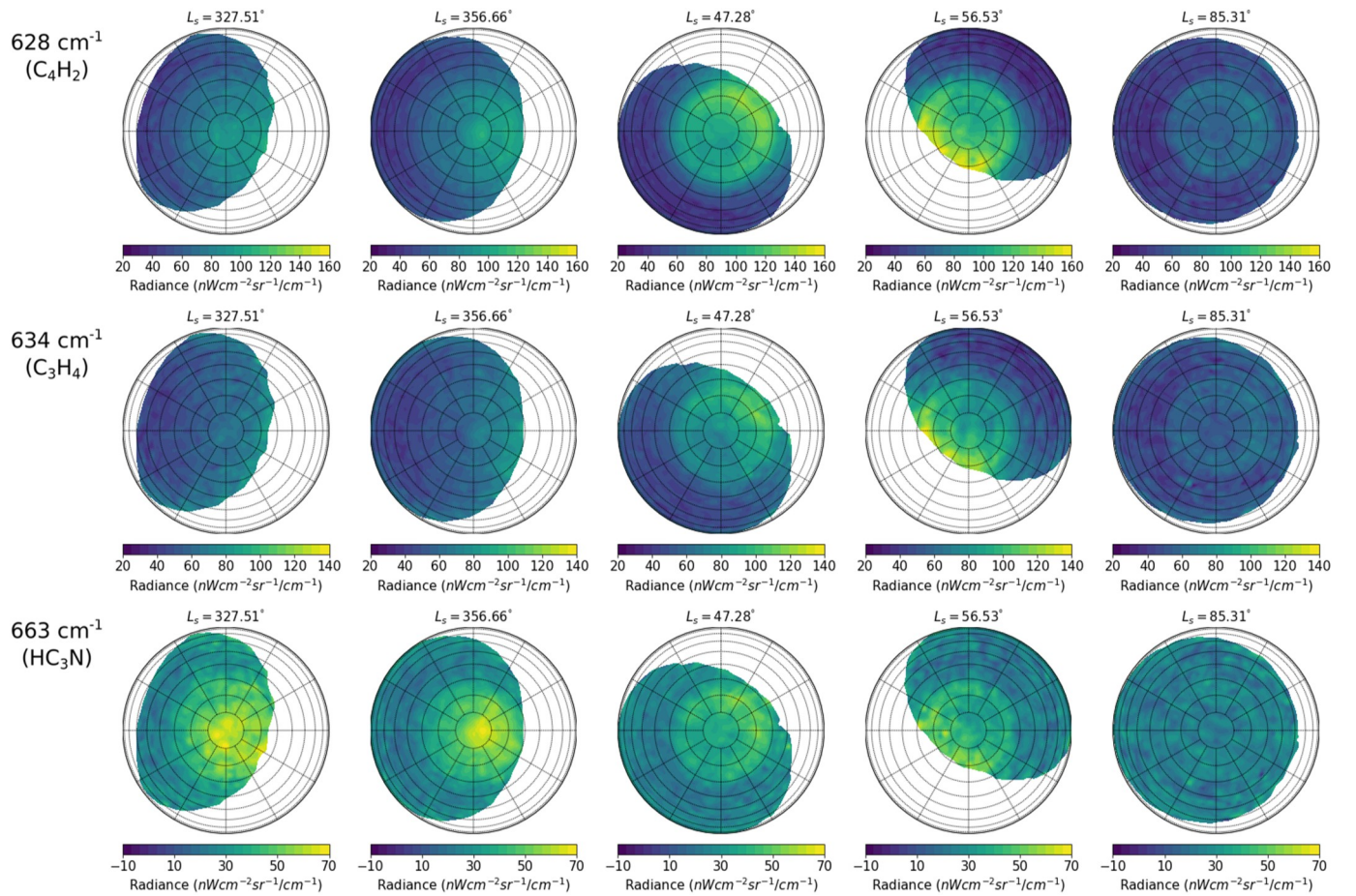


**Fig. 2.** IR emission maps of north pole recorded by CIRS from 2007 (northern winter,  $L_s = 327.51^\circ$ ) to late 2016 (northern summer,  $L_s = 85.31^\circ$ ). Gas emissions are seen to be greatly reduced by summer despite the expected heating of the polar atmosphere, indicating a decrease in gas abundance.

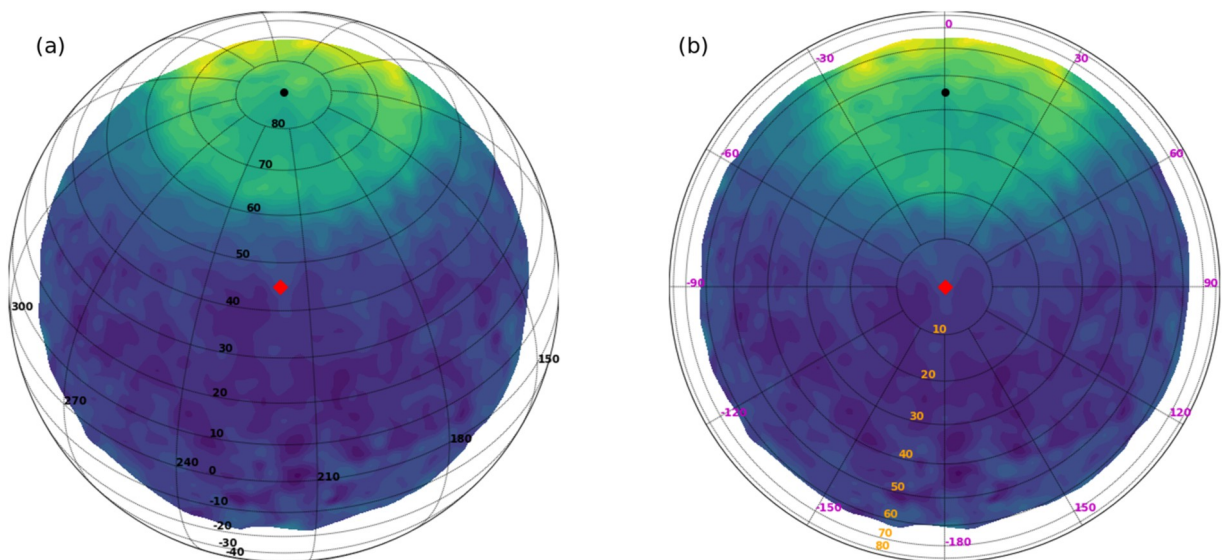


**Fig. 3.** Maps of  $628\text{ cm}^{-1}(\text{C}_4\text{H}_2)$  at  $L_s = 56.53^\circ$  as seen in Fig. 2 in two coordinate frames. (a) Latitude-longitude frame as seen from Cassini with geographic pole marked as a black circle and sub spacecraft point marked as a red diamond and latitudes and longitudes noted in black. (b) Azimuth-angular frame as seen from Cassini with zero azimuth ( $\alpha$ , purple) lies along SPM and emission angle is constant along lines equidistant from zenith ( $\epsilon$ , orange). Limb brightening can be seen as the vortex IR emissions are seen to be greater at larger angular distance (larger emission angle) from Cassini. (For interpretation of the references to color in this figure legend, the reader is referred to the web version of this article.)

the subspacecraft point (zenith). In this frame, emission angle monotonically increases with angular distance from zenith,  $\epsilon$ , whilst having no variation with the azimuth,  $\alpha$ , which has zero defined as the line adjoining the subspacecraft point and the chosen pole position, or spacecraft-pole-meridian (SPM). Fig. 3 illustrates the geometry of the frame change and coordinate system. Since we can only compare values at equal emission angle, we have one less degree of freedom and now are effectively calculating a  $\chi^2$  value for the distribution of emissions either side of the SPM, with  $\chi^2$  for each offset position defined as

$$\chi^2(\phi_p, \theta_p) = \sum_{\epsilon=0}^{\pi/2} \sum_{\alpha=0}^{\pi} \left( \frac{y(\epsilon, \alpha) - y(\epsilon, -\alpha)}{\sqrt{\sigma(\epsilon, \alpha) + \sigma(\epsilon, -\alpha)}} \right)^2$$

where  $\phi_p$  and  $\theta_p$  are the azimuth of the atmospheric pole in the selected reference frame and the offset from the geographic pole respectively,  $y(\epsilon, \alpha)$  is the measured radiance at an angle  $\epsilon$  from zenith and an angle  $\alpha$  from the SPM and  $\sigma(\epsilon, \alpha)$  is the corresponding error.

A limitation of this method is that we can only calculate a  $\chi^2$  profile as a function of  $\alpha$  for each observation. In other words, for any given observation, our minimum  $\chi^2$  value reveals a line originating at the spacecraft along which the best fitting offset position lies. However, combining these  $\chi^2$  values for multiple observations (the sub spacecraft point varies between observations) allows us to calculate the best fitting offset location over the entire mission. This further reduces any bias of limb brightening present in the atmospheric pole estimate. We can also

rotate the azimuths of each  $\chi^2$  profile in order to find the minimum location in any chosen reference frame. Three frames were selected; solar (sub solar point as the reference point), Saturn ( $0^\circ$ W as the reference point) and inertial (sub solar point at equinox as the reference point), with the frame returning the smallest  $\chi^2$  value providing the best fit to the offset.

### 3.2. Retrieval methods

We use the radiative transfer retrieval code, NEMESIS (Irwin et al., 2008) to retrieve continuous temperature profiles and abundances of selected gases from our CIRS spectra. In order to retrieve a parameter, NEMESIS uses a correlated-k based (Lacis and Oinas, 1991) constrained iterative non-linear retrieval method (Rodgers, 1976). Temperature and composition are retrieved by iteratively generating a synthetic spectra and modifying model parameters in order to minimise a cost function between observed and synthetic spectra to give the best fitting model.

Our forward model includes gas abundances measured from a variety of sources. We set the methane abundance to the values measured by the Cassini-Huygens probe GCMS (Niemann et al., 2010) (1.48%). For the remaining trace gases a uniform mixing ratio is assumed above the condensation level using data collected from previous CIRS studies (Coustenis et al., 2007, 2016; de Kok et al., 2007; Flasar et al., 2005).

This study aims to perform retrievals using IR spectra recorded at various latitudes and seasons on Titan. Titan's atmosphere can vary

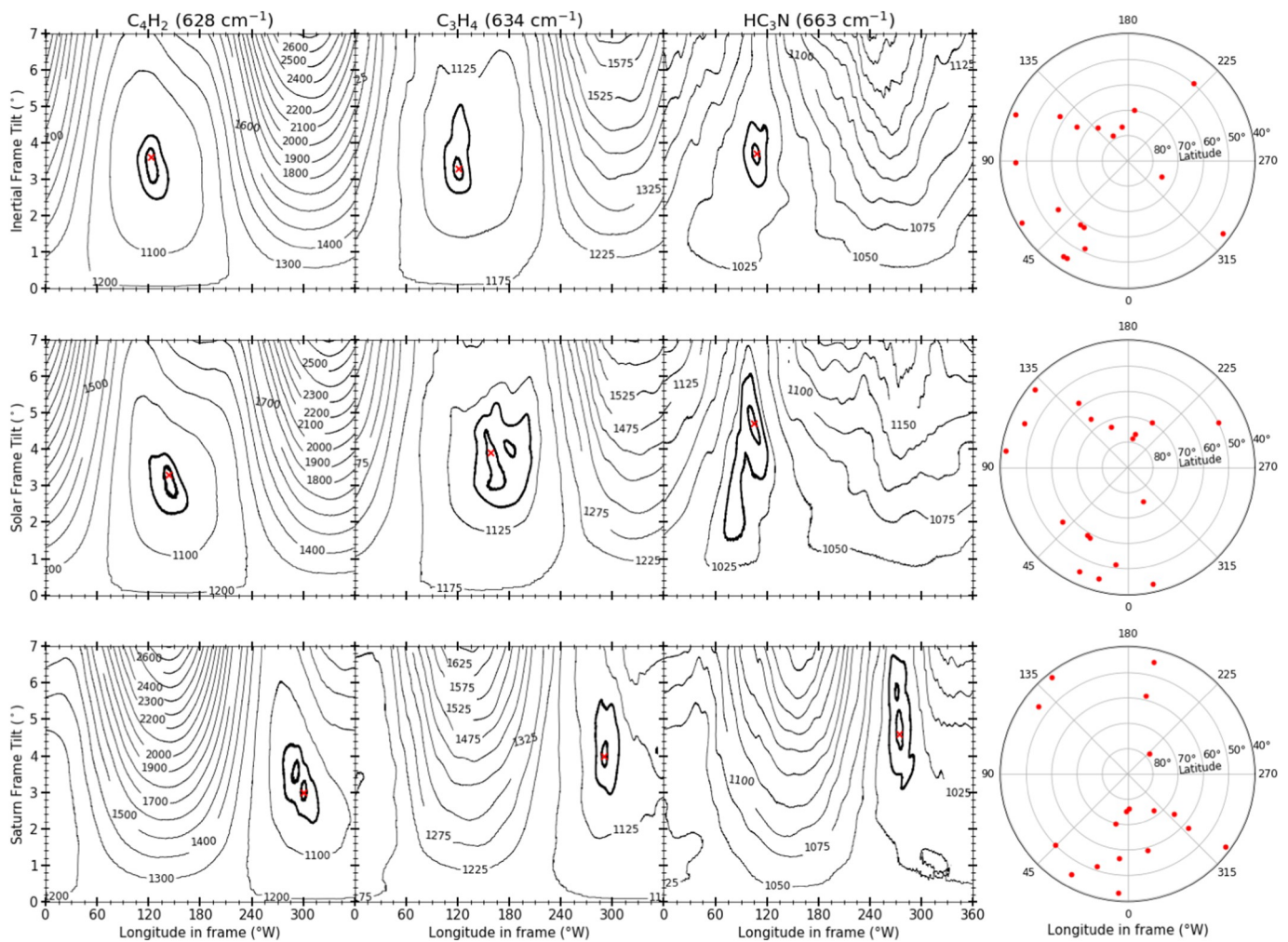


**Fig. 4.** Contour maps of  $\chi^2$  values as a function of tilt and frame longitude for best fitting stratospheric tilt over all 18 observations listed in Table 1.  $\chi^2$  values calculated using emissions from three vortex enriched gases (first 3 columns) are shown in three unique reference frames (rows). Minima are marked with an X and thick contours indicate 1- $\sigma$  and 3- $\sigma$  confidence intervals. Fourth column shows the sub spacecraft points of all observations in each reference frame.



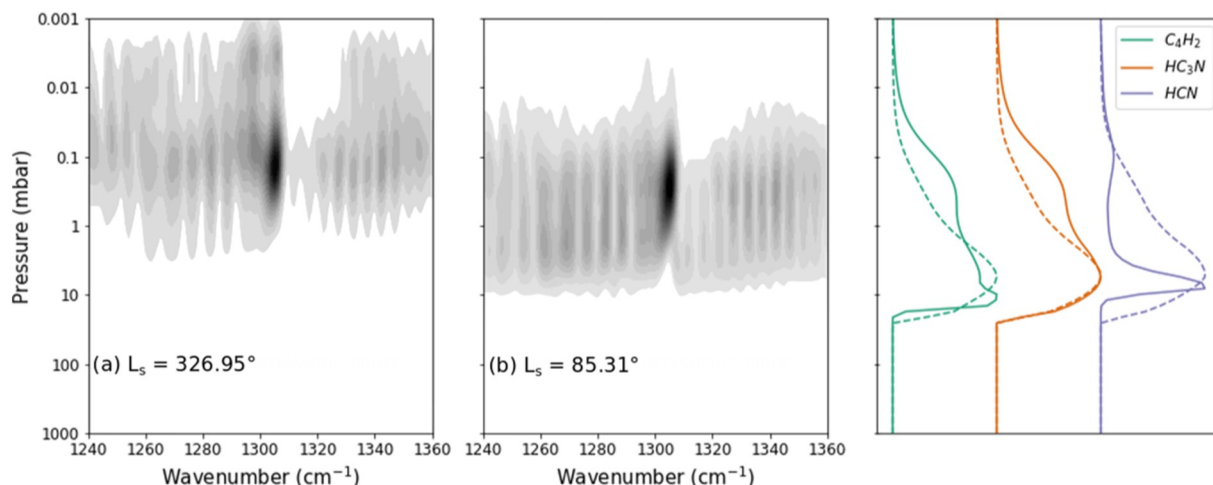


**Fig. 5.** Contribution functions for temperature at the north pole in (a) northern winter and (b) northern summer. Temperature contributions are seen to peak close to 0.1 mbar during the winter, and closer to 1 mbar in the summer. Right panel shows contribution functions for composition at the north pole for northern winter (solid lines) and northern summer (dashed lines).

quite significantly depending on these factors and so to construct a reliable a-priori temperature profile we use the database of temperature profiles from [Teanby et al. \(2019\)](#).

A two stage retrieval process is adopted following [Teanby et al. \(2019\)](#). First, a continuous temperature profile is obtained from the  $\nu_4$   $\text{CH}_4$  band centered about 1240–1360  $\text{cm}^{-1}$  (FP4) for the binned spectra detailed in [Section 2](#). Assuming the  $\text{CH}_4$  abundance to be constant and well mixed throughout the stratosphere allows us to disentangle temperature and composition over this wavenumber range. Second, we perform abundance retrievals over the 620–733  $\text{cm}^{-1}$  range (FP3) by fixing the retrieved temperature profile and scaling the uniform gas profiles. Retrieved properties also have an associated uncertainty, derived from the variance for each wavenumber in the spectrum and an additional forward model error. [Figs. 6 and 7](#) show example fitted spectra for the  $\nu_4$   $\text{CH}_4$  band and FP3 gas emissions respectively.

We can also inspect the regions which our retrievals are sensitive to by examining the contribution functions for selected wavenumbers. The

contribution function is defined as the rate of change of radiance (at a given wavenumber) with respect to the parameter being retrieved. [Fig. 5](#) shows contribution functions for the  $\nu_4$   $\text{CH}_4$  band and  $\text{C}_4\text{H}_2$  (628  $\text{cm}^{-1}$ ),  $\text{HC}_3\text{N}$  (663  $\text{cm}^{-1}$ ) and  $\text{HCN}$  (713  $\text{cm}^{-1}$ ) emissions obtained from spectra recorded near the north pole during winter and summer. The  $\nu_4$  band contribution functions can be seen to peak between the 10–0.001 mbar pressure level depending on latitude and season, indicating that most temperature information originates in this region. The composition contribution functions typically peak between 10–0.01 mbar depending on the latitude, season and photochemical lifetime of the gas species, with a primary peak between 10–1 mbar and a secondary peak near 0.1 mbar caused by the hot stratopause over the polar region ([Teanby et al., 2008b](#)).

### 3.3. Vortex asymmetry

With each observation rotated into the stratospheric tilt frame, we

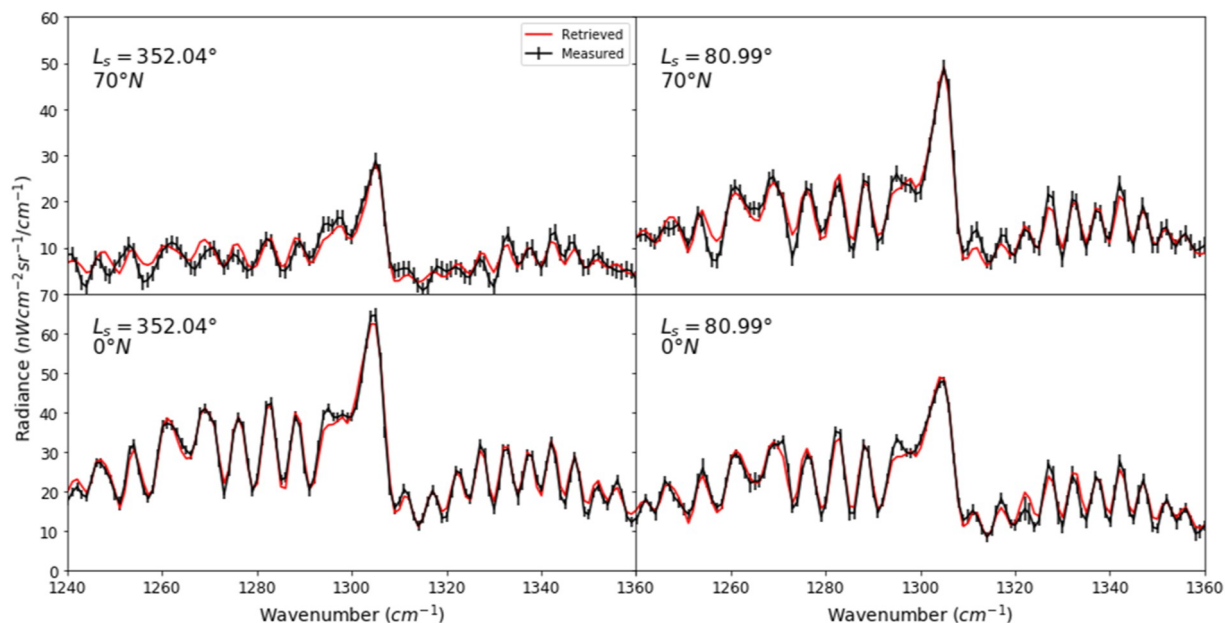


**Fig. 6.** Examples of measured (black) and retrieved (red) spectra for the  $\nu_4$  methane band in FP4 shown near the pole and equator for both northern winter ( $L_s = 352.04^\circ$ ) and northern summer ( $L_s = 80.99^\circ$ ). Continuous temperature profiles are derived from the  $\nu_4$  methane band. (For interpretation of the references to color in this figure legend, the reader is referred to the web version of this article.)

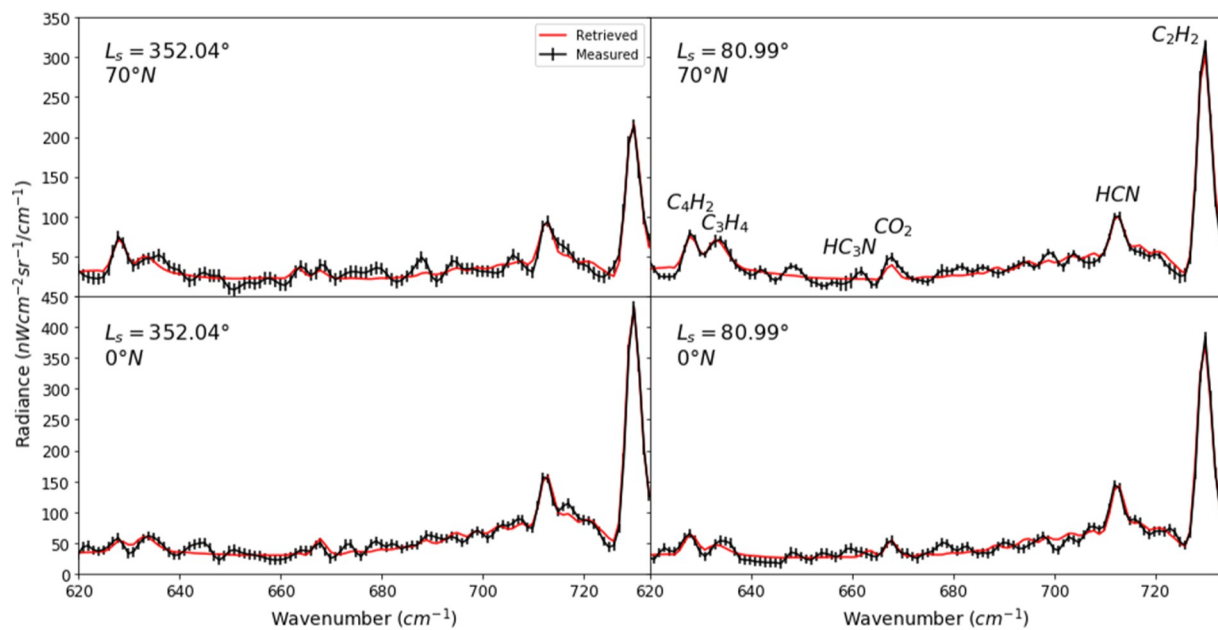


**Fig. 7.** Examples of measured (black) and retrieved (red) spectra in a selected range of FP3 with many gas emissions present, shown near the pole and equator for both northern winter ( $L_s = 352.04^\circ$ ) and northern summer ( $L_s = 80.99^\circ$ ). Emissions for some trace gases such as  $C_4H_2$ ,  $C_3H_4$ ,  $HC_3N$  and  $HCN$  are greater in the polar region than at the equator, particularly during the winter where the polar vortex is strong and gases are more abundant. (For interpretation of the references to color in this figure legend, the reader is referred to the web version of this article.)

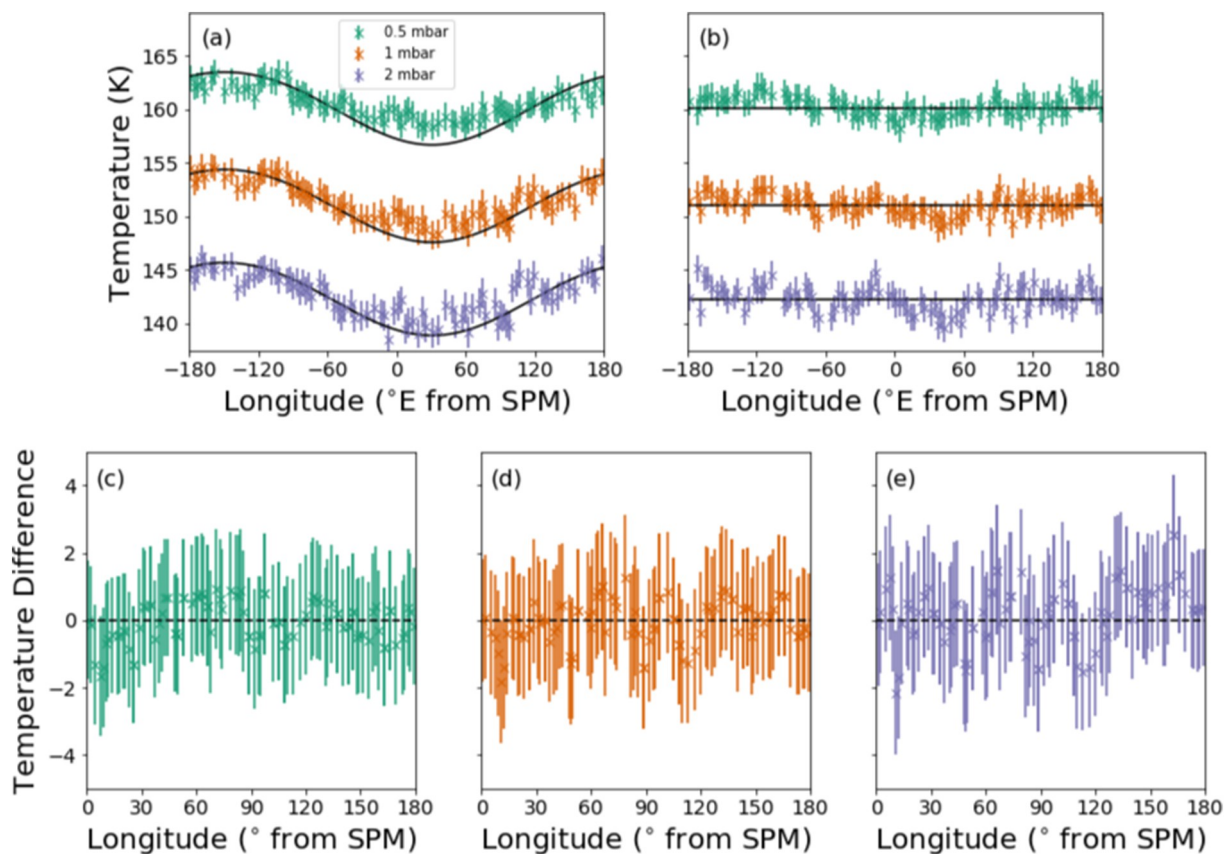


**Fig. 8.** (a) Zonal variation in temperature at 3 pressure levels between  $62\text{--}63^\circ$  N for  $L_s = 356.66^\circ$ . Wavenumber 1 feature can be seen in temperature distribution. (b) Zonal variations in the same latitude band after correction for the stratospheric tilt. Solid black line indicates the best fitting straight line, with (a) showing the best fitting straight line transformed back into the untilted frame. (c), (d) and (e) show the difference in temperature at the 0.5, 1 and 2 mbar levels respectively as a function of unsigned angular distance from the SPM in the tilted frame. The uncertainty on temperatures are derived in the retrieval process. All 3 temperature differences are seen to be distributed around 0 indicating no significant asymmetry in this latitude band.

are now in a position to investigate the zonal variations in temperature and composition of the vortex. We perform the inversion method detailed in Section 3.2 to retrieve continuous temperature profiles and trace gas abundances.

In searching for zonal asymmetry, our analysis must continue to be robust to the effects of viewing geometry. We use a similar method to Section 3.1 where coordinates equidistant from the Spacecraft-pole-meridian (SPM) have the same emission angle, and so are directly comparable. For a zonally symmetric distribution, we expect the difference between these comparable values to be scattered about 0. Fig. 8 illustrates a typical example of temperatures within a latitudinal band spanning  $1^\circ$  which are zonally evenly distributed. We use a  $\chi^2$  method to determine whether or not there is significant variation in each latitude band and therefore the vortex, where  $\chi^2$  is defined as

$$\chi^2(\theta) = \sum_{\phi=0}^{\pi} \left( \frac{y(\phi, \theta) - y(-\phi, \theta)}{\sqrt{\sigma(\phi, \theta) + \sigma(-\phi, \theta)}} \right)^2$$

where  $y(\phi, \theta)$  is the parameter in the selected latitude band,  $\theta$ , at an angle  $\phi$  from the spacecraft-pole meridian, and  $\sigma(\phi, \theta)$  is the error of the parameter. We calculate  $\chi^2$  for each latitude using the parameters retrieved in a  $1^\circ$  latitude band between  $\theta$  and  $\theta + 1^\circ$  such that emission angles remain comparable between measurements.

In the case of our continuous temperature profile retrievals, the retrieval error is used. However, for our scaled abundance profiles the retrieval error only represents the uncertainty of a uniform gas abundance profile for each species, and so does not encapsulate realistic uncertainties on the gas species abundance. To obtain more reliable error estimates, we use values obtained from retrieved limb profiles at the 1 mbar level by Vinatier et al. (2015, 2010). The only gas species which are both present in our retrieval range ( $620\text{--}733\text{ cm}^{-1}$ ) and have limb profiles available are  $C_4H_2$ ,  $HC_3N$  and  $HCN$ . These gases also exhibit the sharpest latitudinal gradients and so are most suitable for looking for asymmetry (Teanby et al., 2019).

## 4. Results

### 4.1. Stratospheric tilt correction

The orientation of the tilt was measured with three trace gas emissions and relative to three reference frames; Saturn, solar and inertial. The minimum  $\chi^2$  values for each offset frame and wavenumber were plotted along with the  $1\text{-}\sigma$  and  $3\text{-}\sigma$  contours and are shown in Fig. 4. In all three frames a tilt of around  $3.5^\circ$  was observed, however the inertial frame resulted in the lowest spread between the best fit pole minimums for each gas emission, and the area covered by the  $3\text{-}\sigma$  bounds appeared to be most compact in the inertial frame. The results for all 3 frames are shown in Table 2. The uncertainties in the three frames are similar, however, when applying the tilts to the asymmetry analysis, the temperature and composition  $\chi^2$  asymmetry values were seen to consistently cross the  $3\text{-}\sigma$  threshold for all but the inertial frame. To investigate the quality of each offset orientation, we examine the zonal asymmetry variation with pressure for each observation, as seen in Fig. 9. Over all observations, the inertial frame is seen to consistently produce no significant asymmetry. However, it does not always produce the least

asymmetry for any given observation. This suggests that whilst the inertial offset provides the best fitting pole location overall, it may not accurately represent the true offset orientation. Each flyby was subsequently rotated into the inertial frame for the vortex asymmetry analysis.

Since the results are dependent on the position of the spacecraft for each observation it is important to ensure there is no sampling bias in any frame. Fig. 4 shows the distribution of the sub spacecraft point with respect to the reference frame for each observation. In all frames the spacecraft positions appear to be well distributed around the pole, suggesting that the results are not skewed in favour of any particular frame.

### 4.2. Vortex asymmetry

To demonstrate the seasonal variation in the vortex temperature and composition, Fig. 10 shows maps of the temperature distribution at the 1 mbar pressure level, and gas abundance distributions for selected gases obtained from retrievals using CIRS data. The binning of data is visible on the maps of Fig. 10 and care should be taken not to interpret the binning grid as an atmospheric structure. Fig. 11 provides quantitative examples of latitudinal variations in the retrieved properties throughout the Cassini mission. Temperature gradients are seen to decrease in the northern summer as the polar stratosphere begins to heat up. Varying gradients in vortex composition are also seen in  $C_4H_2$ ,  $HC_3N$ ,  $HCN$  abundance depending on the season and photochemical lifetime of the gas.

The measure of zonal temperature asymmetry is shown in Fig. 12 which shows the  $\chi^2$  values at various pressure levels in the vortex temperature distribution as a function of latitude for the observations listed in Table 1. The  $\chi^2$  values corresponding to the  $1\text{-}\sigma$  and  $3\text{-}\sigma$  confidence boundaries are also plotted for each latitude.  $1\text{-}\sigma$  and  $3\text{-}\sigma$  values correspond to the  $\chi^2$  required to produce a P-value of 0.3173 and 0.0027 respectively, for  $N - 1$  degrees of freedom where  $N$  is the number of parameters in the latitude band. The temperature distribution in a latitude band is considered to be significantly asymmetric if the calculated value is greater than the  $3\text{-}\sigma$  value. Throughout all 18 observations, there appears to be no significant asymmetry in the vortex temperature at the 0.5, 1 or 2 mbar levels, suggesting that the vortex's temperature distribution is zonally symmetric.

Similarly, Fig. 13 shows the  $\chi^2$  values for zonal asymmetry in the distribution of  $C_4H_2$ ,  $HC_3N$  and  $HCN$  abundance in the vortex as a function of latitude. Amongst the earlier observations we see some zonal variation in the gas abundances northward of around  $50^\circ$  compared to later observations where there is little evidence of variation. This is to be expected since the vortex becomes greatly depleted in trace gas species by the end of the mission, as seen in the abundance maps in Fig. 10 and latitudinal profile examples in Fig. 11. However, at no point during the mission do we see the abundance asymmetry surpassing  $3\text{-}\sigma$ , suggesting that the vortex is also zonally symmetric in its composition.

The method outlined in Section 3.3 would not detect any variations in the temperature or composition which were symmetric about the spacecraft-pole-meridian. However, as seen in Fig. 4, the subspacecraft point is well distributed in longitude around the pole and so it is unlikely such an asymmetry would be absent in all 18 observations.

## 5. Discussion

Despite the ambiguity in the offset orientation, the magnitude of our result is in broad agreement with the previous studies which found the stratospheric tilt to be offset from the pole by  $4.1 \pm 0.2^\circ$ ,  $3.8 \pm 0.9^\circ$ ,  $4.0 \pm 1.5^\circ$  and approximately  $4.5^\circ$  for temperature, haze albedo asymmetry, composition and zonal wind velocity measurements respectively (Achterberg et al., 2008; Roman et al., 2009; Teanby et al., 2010; West et al., 2016). Previously Achterberg et al. (2008) suggested that the tilt is a result of the response of Titan's circulation to solar heating in the

**Table 2**

Results of the atmospheric tilt analysis. Magnitudes in all frames are similar, with the inertial frame giving the most concise errors on magnitude and longitude. Magnitude measured as degrees from geographic pole and longitude measured in  $^\circ\text{W}$  of the reference frame origin.

Reference frame	Offset ( $^\circ$ )	Longitude ( $^\circ\text{W}$ )
Saturn	$3.7 \pm 0.7$	$290 \pm 10$
Solar	$3.5 \pm 0.8$	$125 \pm 30$
Inertial	$3.4 \pm 0.6$	$115 \pm 8$



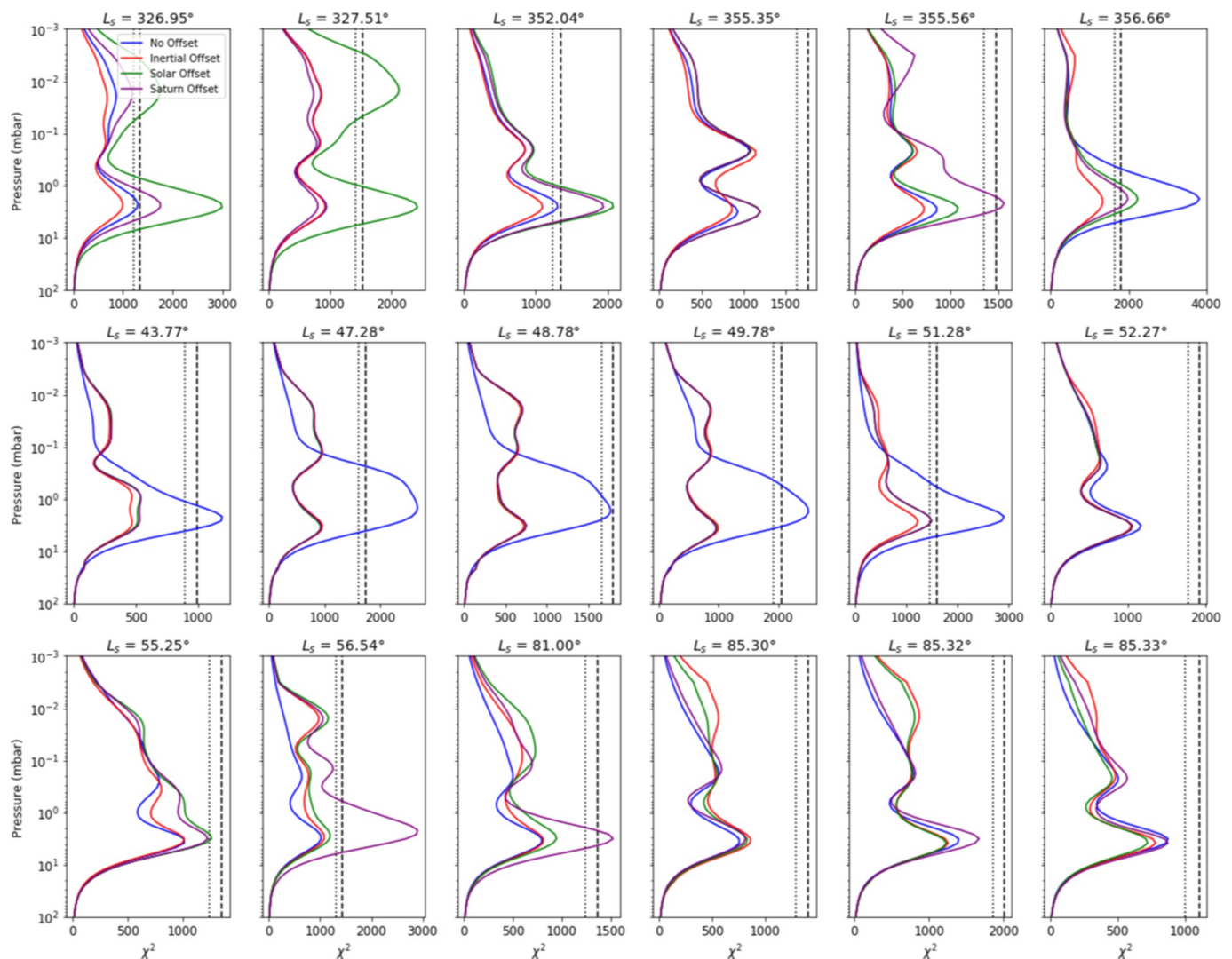


**Fig. 9.** Polar asymmetry of the temperature in the northern hemisphere from 40° northwards. Asymmetry for four offset orientations shown. 1- $\sigma$  and 3- $\sigma$  significance thresholds for asymmetry are shown by the dotted and dashed lines respectively.

atmosphere and so is fixed in the solar frame. Tokano (2010) later predicted a similar offset in their GCM, also noting a westward rotation of the tilt offset with a period of 1 Titan day and varying magnitude with season. They investigate possible mechanisms for the motion of the tilt, proposing that thermal tides cause periodic oscillations in the zonal wind in large parts of the atmosphere which acts to tilt the atmospheric angular momentum vector from the solid body rotation axis. Whilst Saturn's gravitational waves are present on Titan they exhibit a wave-number 2 feature and are much less dominant in the stratosphere than thermal tides, and Rossby waves must propagate with an eastwards group velocity, leaving thermal tides as the most plausible mechanism for this feature. However, Achterberg et al. (2011) later found that the tilt appears to remain stationary in the inertial frame and a small increase in offset magnitude was observed moving into spring, where Tokano (2010) predicted a reduction in magnitude. Furthermore, several studies have suggested that the radiative time constant in Titan's middle atmosphere is short enough that seasonal effects are expected but long enough such that diurnal effects are not expected (Flasar et al., 1981; Lebonnois et al., 2014; Strobel et al., 2010).

Our results make use of data over a wider time period than previous studies, however due to the need to combine multiple datasets to obtain one measurement of the offset position and the relatively few number of datasets available, we can only find the best fitting offset over the entire

Cassini mission. It may be possible that there is indeed a precession of the tilt, which our method would not see due to a lack of temporal resolution. In any case, we search for the stratospheric tilt only to correct our observations so that we can investigate zonal asymmetries in the vortex.

Throughout all 18 observations, we investigate the zonal distributions of temperature at various pressure levels and at no point do we see any signs of significant asymmetry ( $\chi^2$  asymmetry values greater than the 3- $\sigma$  level) as shown in Fig. 12. In some cases the temperature distributions are seen to surpass 1- $\sigma$  suggesting there may be some degree of temperature asymmetry present around the vortex. Similarly, we investigate the zonal distribution of three trace gases;  $C_4H_2$ ,  $HC_3N$  and  $HCN$ . We do not see the  $\chi^2$  asymmetry values to cross the 3- $\sigma$  threshold at any point, indicating that the vortex composition remains uniform zonally.

Comparing Titan's uniform northern vortex with the vortices of other planets may help us better understand what processes govern its evolution. On Earth, similar studies have investigated the size and shape of the northern and southern hemisphere vortices. Mitchell et al. (2013), Waugh and Randel (1999) show that Earth's northern vortex appears to be much more distorted and elongated than the southern vortex. The large variability in vortex shape is attributed to upward propagation of Rossby waves from the troposphere which act to perturb the vortex

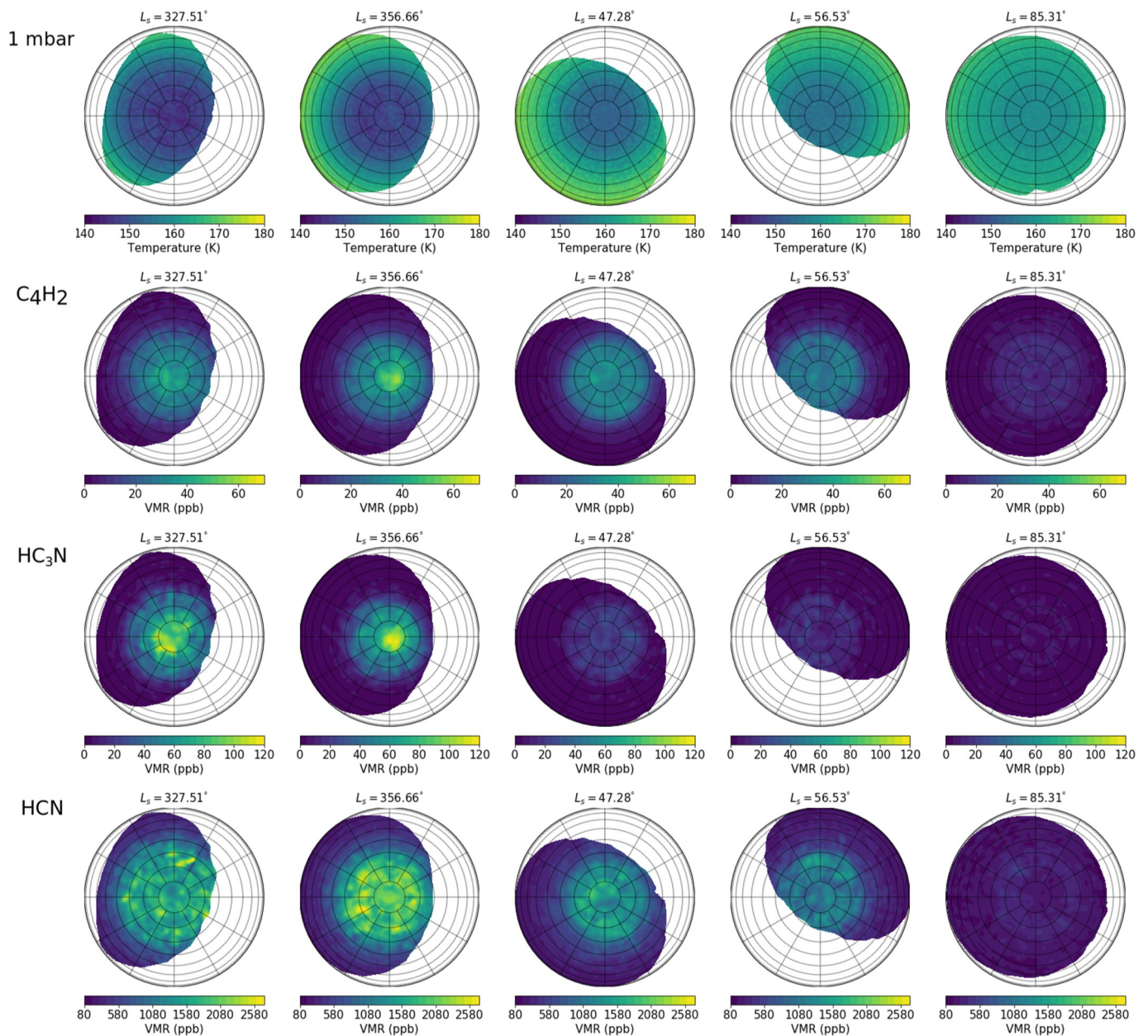


**Fig. 10.** Maps of temperature at 1 mbar and  $C_4H_2$ ,  $HC_3N$ , HCN abundance in the northern hemisphere at various points in the Titan year illustrate the seasonal variations in the vortex.

(Andrews et al., 1987; Mitchell et al., 2015; Waugh and Randel, 1999). Greater variability in the northern hemisphere topography as well as land-sea temperature contrasts results in the generation of stronger planetary waves in the north, weakening the vortex more than in the south. These waves can also contribute to extreme vortex events called Sudden Stratospheric warmings (SSWs) which can see stratospheric temperatures rise by tens of degrees and help to facilitate rapid breakdown of the vortex (Waugh et al., 2016). Similarly, on Mars the southern vortex is seen to be highly variable, more so than in the north (Mitchell et al., 2015; Waugh et al., 2016). The Martian polar atmosphere is also seen to exhibit SSW-like events, or Rapid Polar Warmings (RPWs) (Mitchell et al., 2015), with a variety of factors attributed to their origin. The variable topography in the southern hemisphere generates Rossby waves which can act to perturb the vortex, as on Earth. Inhomogeneities in the atmosphere such as dust storms or  $CO_2$  condensation also have an important effect on the zonal circulation (Guzewich et al., 2016; Newman et al., 2002; Rostami et al., 2018; Toigo et al., 2017). No such SSW

or RPW type event has been observed on Titan.

Titan's topography is relatively flat in comparison to other solar system bodies (Lorenz et al., 2011), suggesting that the generation and upward propagation of strong Rossby waves from the troposphere is less likely than on Earth and Mars. The absence of these planetary waves making their way into the stratosphere could explain how the vortex remains symmetric as it evolves, and the lack of SSW-like events which may otherwise perturb the zonal circulation. Fig. 14 shows a cross section of the mean topography between latitudes where the meridional gradients are typically strongest in the vortices: 50–70° N for Titan and Earth and 50–70° S for Mars. The topographic data was obtained from Cassini Radar measurements for Titan (Lorenz et al., 2013), the USGS GTOPO30 Digital Elevation Model for Earth and the Mars Orbiter Laser Altimeter from the Mars Global Surveyor spacecraft (Smith et al., 2001; Zuber et al., 1992). The elevations are measured as height above sea level (Earth), the difference between planetary radius and the areoid (Mars) and surface height relative to a sphere of radius 2575 km (Titan).



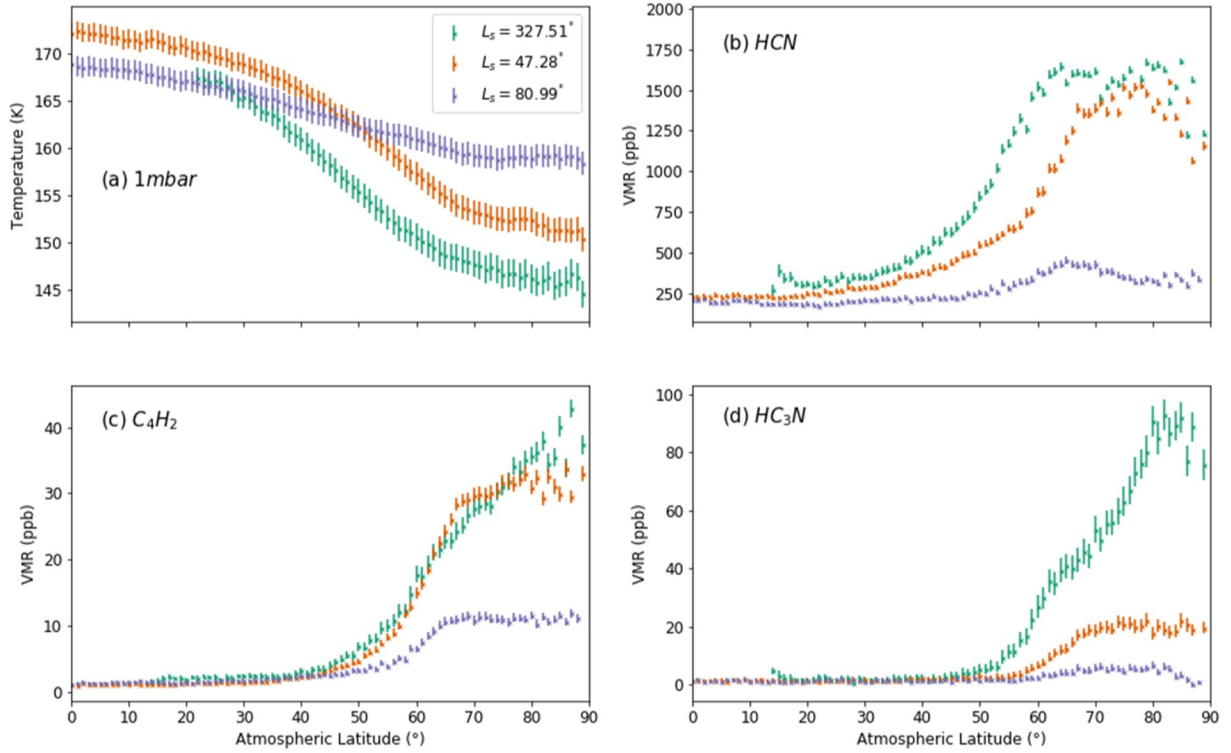


**Fig. 11.** Latitudinal variations in zonal mean temperature and composition in the northern hemisphere for observations at three different times; northern winter (green), early northern summer (orange) and mid northern summer (purple). The uncertainty on temperature and composition are derived in the retrieval process. (For interpretation of the references to color in this figure legend, the reader is referred to the web version of this article.)

An additional factor which may lead to the zonal symmetry is the inability of Rossby waves to propagate vertically into the stratosphere on Titan. Charney and Drazin (1961) demonstrated that the vertical propagation of Rossby waves is dependent on the background flow. For stationary Rossby waves, the Charney-Drazin criterion states that vertical propagation is only possible on the condition that  $0 < u < u_c$ , where  $u$  is the background flow and  $u_c$  is the Rossby critical velocity, with positive velocity defined in the eastward direction.

Assuming a constant background flow, the Rossby critical velocity can be derived from the wave dispersion relation for a Rossby wave and the Quasi-Geostrophic Potential Vorticity relations, and written

$$u_c = \frac{\beta}{k^2 + l^2 + \frac{1}{4L_d^2}}$$

where  $\beta = \frac{\partial f}{\partial y} = \frac{2\Omega \cos \theta}{a}$  is the Rossby parameter, with  $\Omega$ ,  $\theta$  and  $a$  the rotation rate, latitude and radius respectively and  $L_d = \frac{NH}{f}$  is the Rossby deformation Radius with  $N$ ,  $H$  and  $f$  the Brunt-Väisälä frequency, scale height and coriolis frequency respectively and  $k$ ,  $l$  are the zonal and meridional wavenumbers of the wave. Fig. 15 shows the variation of  $u_c$  with zonal wavenumber for Earth, Mars and Titan with meridional wavenumber 0 in the middle-latitudes ( $45^\circ\text{N}$ ).  $N$  was set equal to  $2 \times 10^{-2} \text{ s}^{-1}$  for Earth (Ogura and Phillips, 1962),  $1 \times 10^{-2} \text{ s}^{-1}$  for Mars (the average value between  $45^\circ\text{S}$ – $70^\circ\text{S}$  taken from Ando et al. (2012)) and  $4 \times 10^{-3} \text{ s}^{-1}$  for Titan (Brown et al., 2010). For  $H$ , values of 7 km for Earth (Taylor and J. Lary, 2006), 10 km for Mars (Gierasch and Goody, 1968) and 20 km for Titan (Coustenis and Taylor, 2008) were used. The values of  $H$  and  $N$  used for Titan and Mars are single estimates and are not as well measured as the values for Earth. However, they are used only to predict the typical critical wind speeds in the respective atmospheres and so are adequate for this study. Also plotted are typical zonal wind speeds for each body, with an upper value of  $35 \text{ ms}^{-1}$  near the tropopause for Titan as measured by the Huygens probe (Bird et al.,

2005),  $30 \text{ ms}^{-1}$  for Earth near the tropopause (Hoinka, 1999) and  $20 \text{ ms}^{-1}$  for the lower Martian atmosphere as measured by the Schiaparelli module on the ExoMars rover during descent (Aboudan et al., 2018).

The critical velocity is much larger on Earth and Mars than Titan, indicating that stationary Rossby waves can propagate upwards through a much larger range of wind speeds there. For the longest waves, the largest critical velocity on Titan is seen to be less than  $20 \text{ ms}^{-1}$ . The only in situ measurement of Titan's winds was performed by the Huygens DWE, which recorded a zonal wind profile which increases to greater than  $40 \text{ ms}^{-1}$  at 10 mbar in the lower stratosphere (Bird et al., 2005). GCMs also predict winds in excess of  $40 \text{ ms}^{-1}$  at the 10 mbar level (Lebonnois et al., 2012; Newman et al., 2011). The calculated critical velocity for even the largest wave is much less than the measured and predicted wind speeds in the lower stratosphere. It may be possible then that stationary Rossby waves are unable to propagate vertically in the winds in Titan's stratosphere, and therefore topographically forced stationary Rossby waves do not play a role in the breakup of the polar vortex on Titan. This could lead to a longer lived vortex on Titan than on Earth or Mars and could explain the persistence of Titan's north polar vortex well into northern summer discussed by Teanby et al. (2019).

The northern vortex of Venus is observed to be highly asymmetric with the existence of a 'polar dipole' first identified by Taylor et al. (1979). Yamamoto and Takahashi (2015) suggest that the superposition of a diurnal tide and transient baroclinic waves in the polar region can create irregular vortex shapes. As mentioned previously, Titan's middle atmosphere is not expected to be sensitive to diurnal effects. Leovy and Pollack (1973) first showed that the combination of Titan's slow rotation rate and large Rossby radius of deformation (comparable to its radius) produce conditions in which baroclinic waves cannot efficiently transport heat, and that axisymmetric meridional circulations dominate. Mitchell and Vallis (2010) later demonstrated that baroclinic instability is unable to form in a superrotating atmosphere, suggesting that baroclinic waves should not be present in the atmosphere of Titan or Venus.



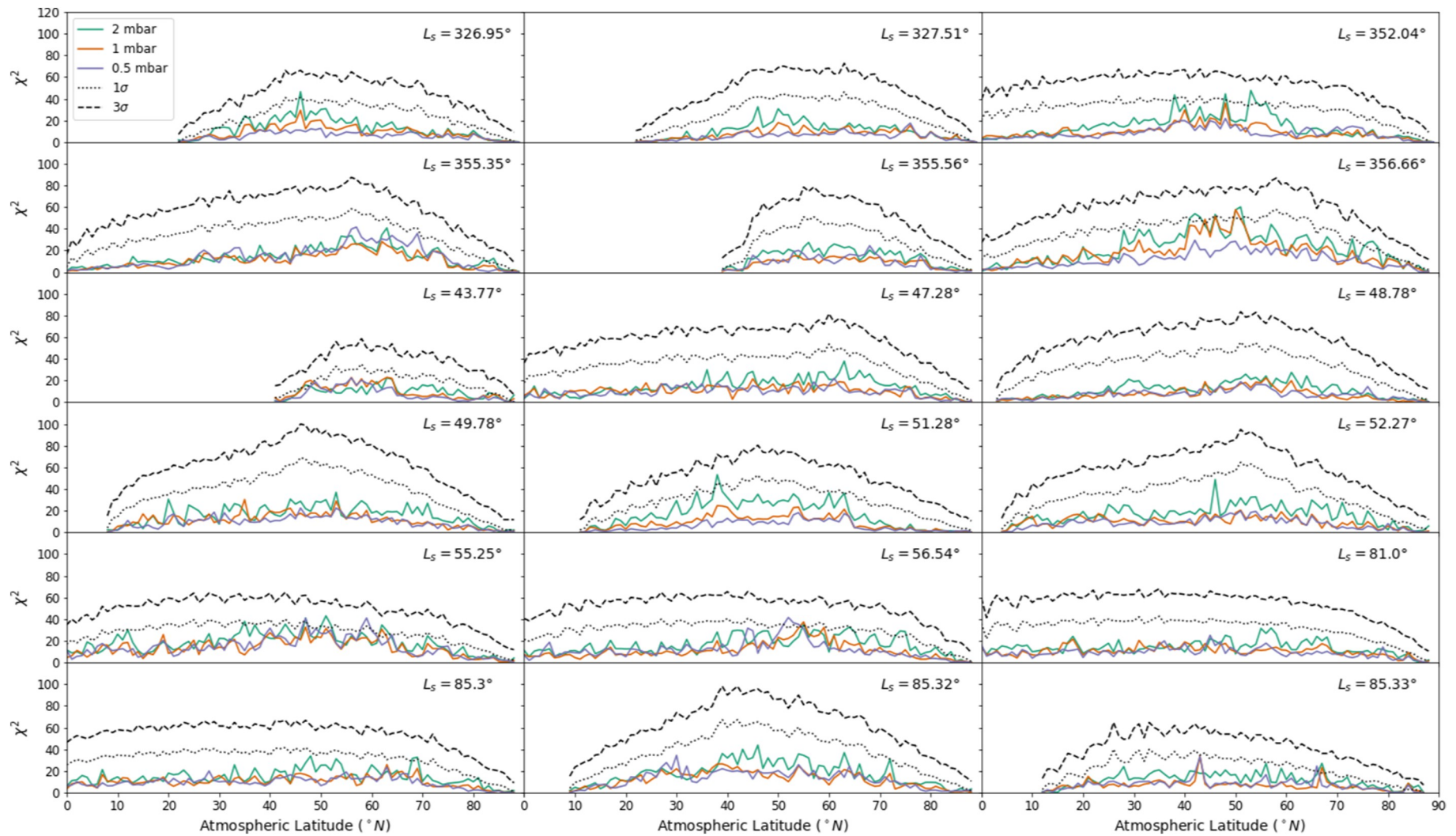


**Fig. 12.**  $\chi^2$  values calculated at all latitudes in northern hemisphere for temperatures at 3 pressure levels and all selected observations. 1- $\sigma$  and 3- $\sigma$  confidence boundary also shown as dotted and dashed black lines respectively.

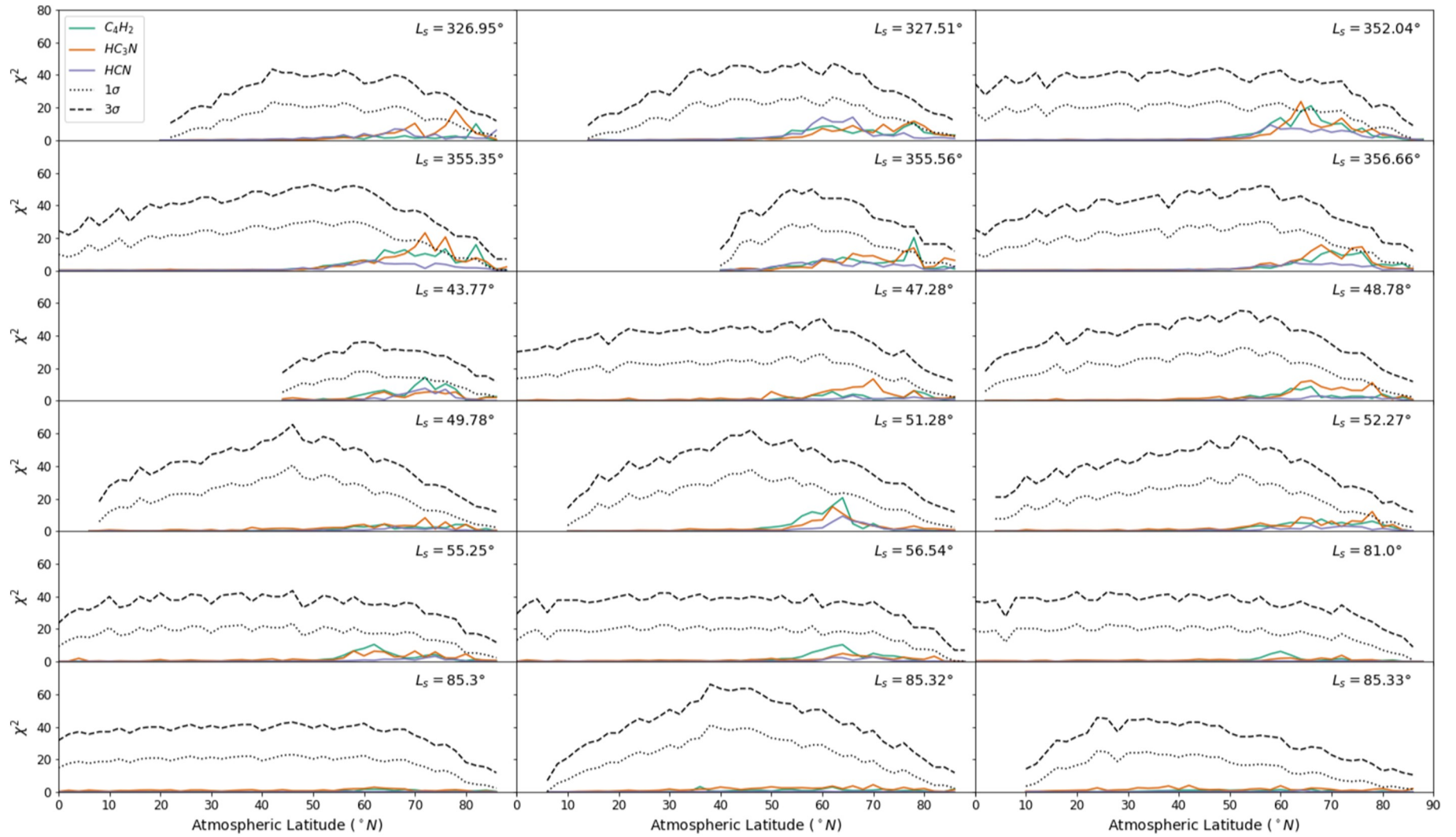


Fig. 13. Similar to Fig. 12, but with  $\chi^2$  values for composition asymmetry.

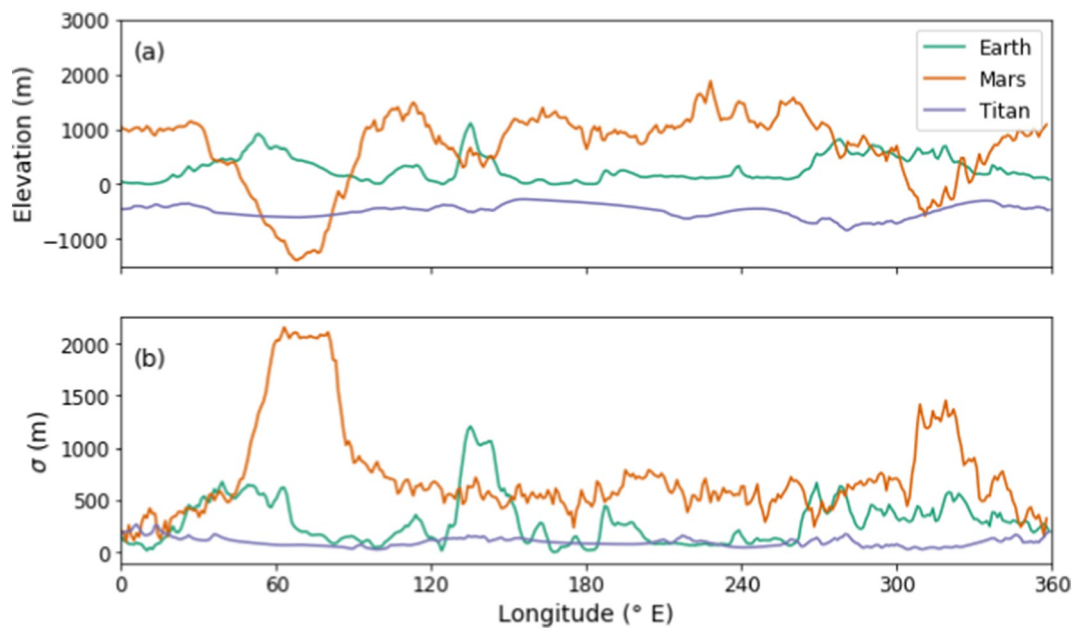


Fig. 14. (a) Mean topography for Titan and Earth between  $50^{\circ}$ – $70^{\circ}$ N and Mars between  $50^{\circ}$ – $70^{\circ}$ S. (b) Standard deviation of the topography.

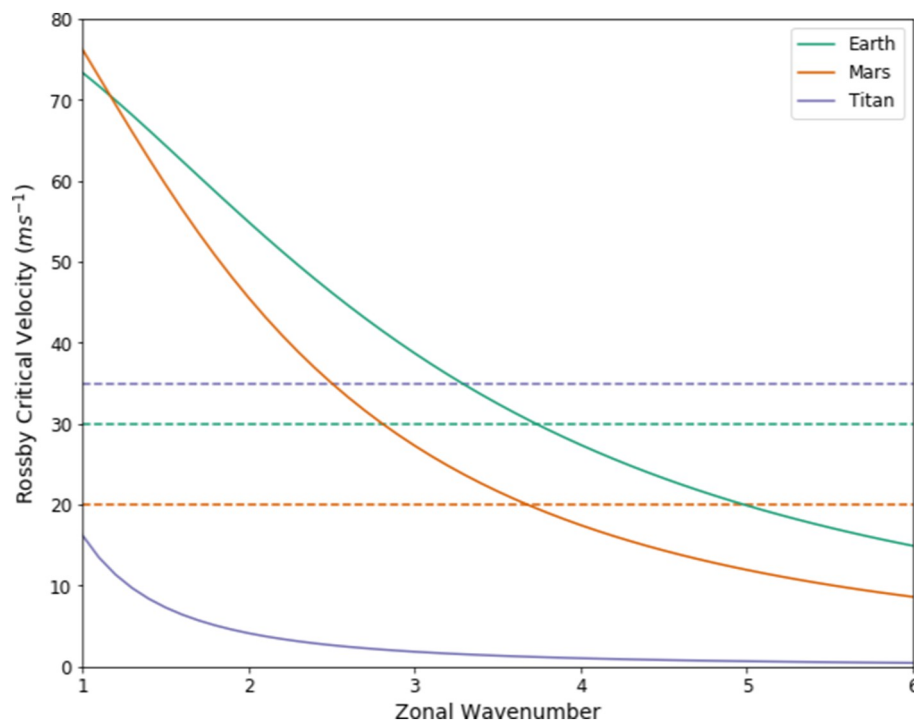


Fig. 15. Variation of the Rossby critical velocity with zonal wavenumber for a Rossby wave with a meridional wavenumber of 0 for Earth, Mars and Titan. Typical zonal wind speeds in the lower atmosphere shown as dashed lines.

However, Sugimoto et al. (2014) argue that on Venus the instability is formed at the cloud level, leading to the generation of such waves. Whilst the conditions for baroclinic instability are not expected to be met in superrotating atmospheres in general, if there is a mechanism producing it on Venus but not Titan it may offer an explanation as to the differences in their vortices.

Topographically forced Rossby waves are not the only mechanism which could contribute to the break up of the polar vortex. Teanby et al. (2008a) noted an increase in abundance of HCN,  $\text{C}_2\text{H}_2$  and  $\text{C}_4\text{H}_2$  extending from the vortex region towards the equator at altitudes of

around 200–300 km ( $\approx 1$ – $0.1$  mbar). They suggest that horizontal mixing by gravity waves and barotropic instabilities are responsible. Lorenz et al. (2014) later identified the existence of internal gravity waves in Titan's lower stratosphere using Huygens in situ measurements. Wavelengths of 3–8 km and amplitudes of 3 K were indicated. They noted that Titan's zonal winds likely form a critical layer for the upward propagation of gravity waves, with the 8 km waves as the dominant wave above the critical layer. Whilst such gravity waves may play a role in the breakup for the vortex, the CIRS nadir observations used in this analysis is unlikely to be able to resolve them due to their small vertical scales



and fine zonal structure, however CIRS limb data may be adequate to investigate the influence of such waves on the vortex breakup. Furthermore, although [Teanby et al. \(2008a\)](#) suggest barotropic instabilities may be present and important for transporting gases from the vortex towards the equator, the lack of asymmetry in the temperature and composition across the vortex indicate that such instabilities are not resolvable with CIRS nadir data, even if they are present.

## 6. Conclusion

In this study, we used 18 CIRS nadir mapping observations covering half a Titan year to investigate the evolution of Titan's northern polar vortex. Using IR gas emissions in the vortex region we found the stratospheric rotation axis to be offset from the solid body rotation axis by  $3.4 \pm 0.6^\circ$ , in broad agreement with previous studies which found values of  $4.1 \pm 0.2^\circ$ ,  $3.8 \pm 0.9^\circ$ ,  $4.0 \pm 1.5^\circ$  and approximately  $4.5^\circ$  ([Achterberg et al., 2008](#); [Roman et al., 2009](#); [Teanby et al., 2010](#); [West et al., 2016](#)), although peculiarly find the level of asymmetry in the vortex is minimised when the offset is fixed in an inertial frame. However, examination of the level of asymmetry present in each observation after correction for the offset indicates that at times the quality of the inertial frame fit is indistinguishable from the solar or Saturn fixed-frames. This suggests we cannot rule out precession of the atmospheric symmetry axis.

By producing temperature and composition maps of the northern polar regions we also find that the vortex shows no sign of significant zonal variations in temperature or gas abundance at any point, and remains broadly axisymmetric in shape as it evolves and breaks up, uniformly increasing or decreasing in size throughout its lifetime. This suggests Titan's vortex behaves differently to those on Earth, Mars and Venus. Alongside seasonal radiation changes, an important factor in the breakup of the polar vortex on Earth is mixed Rossby-gravity waves which can be produced by large scale topography and land-sea contrasts. Similarly, the breakup of the polar vortex on Mars is influenced by seasonal radiation changes and dust and CO<sub>2</sub> variability in the atmosphere which absorb short wave radiation causing rapid warming of the vortex. The relatively flat topography of Titan and the fast superrotating zonal winds produce unfavourable conditions for the upward propagation of Rossby waves into the stratosphere where they could disturb the vortex. Venus' atmosphere is also superrotating, but strong thermal tides and possible baroclinic waves act to perturb the zonal flow. Long radiative timescales in Titan's stratosphere likely prevent such diurnal tides and baroclinic waves are not expected to form. Other wave mechanisms such as gravity waves may play a role in the breakup of the vortex on a finer scale, but no large scale Rossby waves appear to perturb the vortex. This could explain the long duration of Titan's northern polar vortex observed by Cassini ([Teanby et al., 2019](#)) and the high degree of zonal symmetry we observe.

## Acknowledgments

This work was funded by the UK Science and Technology Facilities Council (STFC).

## References

- Aboudan, A., Colombatti, G., Bettanini, C., Ferri, F., Lewis, S., Van Hove, B., Karatekin, O., Debei, S., 2018. ExoMars 2016 Schiaparelli module trajectory and atmospheric profiles reconstruction. Analysis of the on-board inertial and radar measurements. *Space Sci. Rev.* 214, 97. Aug.
- Achterberg, R.K., Conrath, B.J., Gierasch, P.J., Flasar, F.M., Nixon, C.A., 2008. Observation of a tilt of Titan's middle-atmospheric superrotation. *Icarus* 197, 549–555. Oct.
- Achterberg, R.K., Gierasch, P.J., Conrath, B.J., Michael Flasar, F., Nixon, C.A., 2011. Temporal variations of Titan's middle-atmospheric temperatures from 2004 to 2009 observed by Cassini/CIRS. *Icarus* 211, 686–698. Jan.
- Ando, H., Imamura, T., Tsuda, T., 2012. Vertical wavenumber spectra of gravity waves in the Martian atmosphere obtained from Mars global surveyor radio occultation data. *J. Atmos. Sci.* 69, 2906–2912.
- Andrews, D.G., Holton, J.R., Leovy, C.B., 1987. *Middle Atmosphere Dynamics*. Academic Press, London.
- Bird, M.K., Allison, M., Asmar, S.W., Atkinson, D.H., Avruce, I.M., Dutta-Roy, R., Dziemba, Y., Edenhofer, P., Folkner, W.M., Gurvits, L.I., Johnston, D.V., Plettemeier, D., Pogrebenko, S.V., Preston, R.A., Tyler, G.L., 2005. The vertical profile of winds on Titan. *Nature* 438, 800–802. Dec.
- Brown, R.H., Lebreton, J.-P., Waite, J.H., 2010. *Titan From Cassini-Huygens*. Springer.
- Charney, J.G., Drazin, P.G., 1961. Propagation of planetary-scale disturbances from the lower into the upper atmosphere. *J. Geophys. Res.* 66, 83–109. Jan.
- Coustenis, A., Achterberg, R.K., Conrath, B.J., Jennings, D.E., Marten, A., Gautier, D., Nixon, C.A., Flasar, F.M., Teanby, N.A., Bézard, B., Samuelson, R.E., Carlson, R.C., Lellouch, E., Bjoraker, G.L., Romani, P.N., Taylor, F.W., Irwin, P.G.J., Fouchet, T., Hubert, A., Orton, G.S., Kunde, V.G., Vinatier, S., Mondellini, J., Abbas, M.M., Courtin, R., 2007. The composition of Titan's stratosphere from Cassini/CIRS mid-infrared spectra. *Icarus* 189, 35–62. Jul.
- Coustenis, A., Jennings, D.E., Achterberg, R.K., Bampasidis, G., Lavvas, P., Nixon, C.A., Teanby, N.A., Anderson, C.M., Cottini, V., Flasar, F.M., 2016. Titan's temporal evolution in stratospheric trace gases near the poles. *Icarus* 270, 409–420. May.
- Coustenis, A., Taylor, F.W., 2008. *Titan: Exploring an Earthlike World.*, Second edition vol. 4. World Scientific Publishing Company.
- de Kok, R., Irwin, P.G.J., Teanby, N.A., Nixon, C.A., Jennings, D.E., Fletcher, L., Howett, C., Calcutt, S.B., Bowles, N.E., Flasar, F.M., Taylor, F.W., 2007. Characteristics of Titan's stratospheric aerosols and condensate clouds from Cassini CIRS far-infrared spectra. *Icarus* 191, 223–235. Nov.
- Flasar, F.M., Achterberg, R.K., 2009. The structure and dynamics of Titan's middle atmosphere. *Philos. Trans. R. Soc. London A* 367, 649–664. Feb.
- Flasar, F.M., Achterberg, R.K., Conrath, B.J., Gierasch, P.J., Kunde, V.G., Nixon, C.A., Bjoraker, G.L., Jennings, D.E., Romani, P.N., Simon-Miller, A.A., Bézard, B., Coustenis, A., Irwin, P.G.J., Teanby, N.A., Brasunas, J., Pearl, J.C., Segura, M.E., Carlson, R.C., Mamoutkine, A., Schinder, P.J., Barucci, A., Courtin, R., Fouchet, T., Gautier, D., Lellouch, E., Marten, A., Prangé, R., Vinatier, S., Strobel, D.F., Calcutt, S.B., Read, P.L., Taylor, F.W., Bowles, N., Samuelson, R.E., Orton, G.S., Spilker, L.J., Owen, T.C., Spencer, J.R., Showalter, M.R., Ferrari, C., Abbas, M.M., Raulin, F., Edgington, S., Ade, P., Wishnow, E.H., 2005. Titan's atmospheric temperatures, winds, and composition. *Science* 308, 975–978. May.
- Flasar, F.M., Kunde, V.G., Abbas, M.M., Achterberg, R.K., Ade, P., Barucci, A., Bézard, B., Bjoraker, G.L., Brasunas, J.C., Calcutt, S., Carlson, R., Césarsky, C.J., Conrath, B.J., Coradini, A., Courtin, R., Coustenis, A., Edberg, S., Edgington, S., Ferrari, C., Fouchet, T., Gautier, D., Gierasch, P.J., Grossman, K., Irwin, P., Jennings, D.E., Lellouch, E., Mamoutkine, A.A., Marten, A., Meyer, J.P., Nixon, C.A., Orton, G.S., Owen, T.C., Pearl, J.C., Prangé, R., Raulin, F., Read, P.L., Romani, P.N., Samuelson, R.E., Segura, M.E., Showalter, M.R., Simon-Miller, A.A., Smith, M.D., Spencer, J.R., Spilker, L.J., Taylor, F.W., 2004. Exploring the Saturn system in the thermal infrared: the composite infrared spectrometer. *Space Sci. Rev.* 115, 169–297. Dec.
- Flasar, F.M., Samuelson, R.E., Conrath, B.J., 1981. Titan's atmosphere: temperature and dynamics. *Nature* 292, 693–698. Aug.
- Fulchignoni, M., Ferri, F., Angrilli, F., Ball, A.J., Bar-Nun, A., Barucci, M.A., Bettanini, C., Bianchini, G., Borucki, W., Colombatti, G., Coradini, M., Coustenis, A., Debei, S., Falkner, P., Fanti, G., Flamini, E., Gaborit, V., Grard, R., Hamelin, M., Harri, A.M., Hathi, B., Jernej, I., Leese, M.R., Lehto, A., Lion Stoppato, P.F., López-Moreno, J.J., Mäkinen, T., McDonnell, J.A.M., McKay, C.P., Molina-Cuberos, G., Neubauer, F.M., Pirronello, V., Rodrigo, R., Saggini, B., Schwingenschuh, K., Seiff, A., Simões, F., Svedhem, H., Tokano, T., Townner, M.C., Trautner, R., Withers, P., Zarnecki, J.C., 2005. In situ measurements of the physical characteristics of Titan's environment. *Nature* 438, 785–791. Dec.
- Gierasch, P., Goody, R., 1968. A study of the thermal and dynamical structure of the Martian lower atmosphere. *Planet Space Sci.* 16, 615–646. May.
- Guzewich, S.D., Toigo, A., Waugh, D., 2016. The effect of dust on the Martian polar vortices. *Icarus* 278, 100–118.
- Hoinka, K.P., 1999. Temperature, humidity, and wind at the global tropopause. *Mon. Weather Rev.* 127, 2248. Jan.
- Hourdin, F., Talagrand, O., Sadourny, R., Courtin, R., Gautier, D., McKay, C.P., 1995. Numerical simulation of the general circulation of the atmosphere of Titan. *Icarus* 117, 358–374. Oct.
- Irwin, P.G.J., Teanby, N.A., de Kok, R., Fletcher, L.N., Howett, C.J.A., Tsang, C.C.C., Wilson, C.F., Calcutt, S.B., Nixon, C.A., Parrish, P.D., 2008. The NEMESIS planetary atmosphere radiative transfer and retrieval tool. *J. Quant. Spectrosc. Radiat. Transf.* 109, 1136–1150. Apr.
- Jennings, D.E., Flasar, F.M., Kunde, V.G., Nixon, C.A., Segura, M.E., Romani, P.N., Gorius, N., Albright, S., Brasunas, J.C., Carlson, R.C., Mamoutkine, A.A., Guandique, E., Kaelberer, M.S., Aslam, S., Achterberg, R.K., Bjoraker, G.L., Anderson, C.M., Cottini, V., Pearl, J.C., Smith, M.D., Hesman, B.E., Barney, R.D., Calcutt, S., Vellacott, T.J., Spilker, L.J., Edgington, S.G., Brooks, S.M., Ade, P., Schinder, P.J., Coustenis, A., Courtin, R., Michel, G., Fetting, R., Pílorz, S., Ferrari, C., 2017. Composite infrared spectrometer (cirs) on Cassini. *Appl. Opt.* 56, 5274–5294. Jun.
- Krasnopolsky, V.A., 2009. A photochemical model of Titan's atmosphere and ionosphere. *Icarus* 201, 226–256. May.
- Lacis, A.A., Oinas, V., 1991. A description of the correlated-k distribution method for modelling nongray gaseous absorption, thermal emission, and multiple scattering in vertically inhomogeneous atmospheres. *J. Geophys. Res.* 96, 9027–9064. May.
- Lavvas, P.P., Coustenis, A., Vardavas, I.M., 2008. Coupling photochemistry with haze formation in Titan's atmosphere, part II: results and validation with Cassini/Huygens data. *Planet. Space Sci.* 56, 67–99. Jan.

- Lebonnois, S., Burgalat, J., Rannou, P., Charnay, B., 2012. Titan global climate model: a new 3-dimensional version of the IPSL Titan GCM. *Icarus* 218, 707–722. Mar.
- Lebonnois, S., Flasar, F.M., Tokano, T., Newman, C.E., 2014. Titan: Interior, Surface, Atmosphere, and Space Environment, Cambridge Planetary Science. Ch. The general circulation of Titan's lower and middle atmosphere. Cambridge University Press, pp. 122–157.
- Leovy, C.B., Pollack, J.B., 1973. A first look at atmospheric dynamics and temperature variations on Titan. *Icarus* 19, 195–201. Jun.
- Lorenz, R.D., Stiles, B.W., Aharonson, O., Lucas, A., Hayes, A.G., Kirk, R.L., Zebker, H.A., Turtle, E.P., Neish, C.D., Stofan, E.R., Barnes, J.W., 2013. A global topographic map of Titan. *Icarus* 225, 367–377. Jul.
- Lorenz, R.D., Turtle, E.P., Stiles, B., Le Gall, A., Hayes, A., Aharonson, O., Wood, C.A., Stofan, E., 2011. Hypsometry of Titan. *Icarus* 211, 699–706. Jan.
- Lorenz, R.D., Young, L.A., Ferri, F., 2014. Gravity waves in Titan's lower stratosphere from Huygens probe in situ temperature measurements. *Icarus* 227, 49–55. Jan.
- Mitchell, D., Montabone, L., Thomson, S., Read, P., 2015. Polar vortices on earth and mars: a comparative study of the climatology and variability from reanalyses. *Q. J. R. Meteorol. Soc.* 141, 550–562.
- Mitchell, D.M., Gray, L.J., Anstey, J., Baldwin, M.P., Charlton-Perez, A.J., 2013. The influence of stratospheric vortex displacements and splits on surface climate. *J. Clim.* 26, 2668–2682.
- Mitchell, J.L., Vallis, G.K., 2010. The transition to superrotation in terrestrial atmospheres. *J. Geophys. Res. (Planets)* 115, E12008. Dec.
- Newman, C.E., Lee, C., Lian, Y., Richardson, M.I., Toigo, A.D., 2011. Stratospheric superrotation in the TitanWRF model. *Icarus* 213, 636–654. Jun.
- Newman, C.E., Lewis, S.R., Read, P.L., Forget, F., 2002. Modeling the Martian dust cycle 2. Multiannual radiatively active dust transport simulations. *J. Geophys. Res. (Planets)* 107, 5124. Dec.
- Niemann, H.B., Atreya, S.K., Demick, J.E., Gautier, D., Haberman, J.A., Harpold, D.N., Kasprzak, W.T., Lunine, J.I., Owen, T.C., Raulin, F., 2010. Composition of Titan's lower atmosphere and simple surface volatiles as measured by the Cassini-Huygens probe gas chromatograph mass spectrometer experiment. *J. Geophys. Res. (Planets)* 115, E12006. Dec.
- Nixon, C.A., Anstey, T.M., Lombardo, N.A., Bjoraker, G.L., Achterberg, R.K., Annex, A.M., Rice, M., Romani, P.N., Jennings, D.E., Samuelson, R.E., Anderson, C.M., Coustenis, A., Bézard, B., Vinatier, S., Lellouch, E., Courtin, R., Teanby, N.A., Cottini, V., Flasar, F.M., 2019. Cassini Composite Infrared Spectrometer (CIRS) observations of Titan 2004–2017. *arXiv e-prints*. [arXiv:1907.12612](https://arxiv.org/abs/1907.12612). Jul.
- Ogura, Y., Phillips, N.A., 1962. Scale analysis of deep and shallow convection in the atmosphere. *J. Atmos. Sci.* 19, 173–179. Mar.
- Rodgers, C.D., 1976. Retrieval of atmospheric temperature and composition from remote measurements of thermal radiation. *Rev. Geophys. Space Phys.* 14, 609. Nov.
- Roman, M.T., West, R.A., Banfield, D.J., Gierasch, P.J., Achterberg, R.K., Nixon, C.A., Thomas, P.C., 2009. Determining a tilt in Titan's north-south albedo asymmetry from Cassini images. *Icarus* 203, 242–249. Sep.
- Rostami, M., Zeitlin, V., Montabone, L., 2018. On the role of spatially inhomogeneous diabatic effects upon the evolution of Mars' annular polar vortex. *Icarus* 314, 376–388. Nov.
- Smith, D.E., Zuber, M.T., MOLA Science Team, 2001. A Mars' year of topographic mapping with the Mars orbiter laser altimeter. In: *Lunar and Planetary Science Conference*, p. 1959. Mar.
- Strobel, D.F., Atreya, S.K., Bézard, B., Ferri, F., Flasar, F.M., Fulchignoni, M., Lellouch, E., Müller-Wodarg, I., 2010. Titan from Cassini-Huygens. Ch. Atmospheric Structure and Composition. Springer, p. 235.
- Sugimoto, N., Takagi, M., Matsuda, Y., 2014. Baroclinic instability in the Venus atmosphere simulated by GCM. *J. Geophys. Res. (Planets)* 119, 1950–1968. Aug.
- Sylvestre, M., Teanby, N.A., Vatan, d'Ollone, J., Vinatier, S., Bézard, B., Lebonnois, S., Irwin, P.G.J., 2019. Seasonal evolution of temperatures in Titan's lower stratosphere. *arXiv e-prints*. [arXiv:1902.01841](https://arxiv.org/abs/1902.01841). Feb.
- Sylvestre, M., Teanby, N.A., Vinatier, S., Lebonnois, S., Irwin, P.G.J., 2018. Seasonal Evolution of C<sub>2</sub>N<sub>2</sub>, C<sub>3</sub>H<sub>4</sub>, and C<sub>4</sub>H<sub>2</sub> Abundances in Titan's Lower Stratosphere, 609. A&A, p. A64. Jan.
- Taylor, F., Lary, D.J., 2006. Elementary climate physics. *Physics Today - PHYS TODAY* 59, 07.
- Taylor, F.W., Diner, D.J., Elson, L.S., McCleese, D.J., Martonchik, J.V., Delderfield, J., Bradley, S.P., Schofield, J.T., Gille, J.C., Coffey, M.T., 1979. Temperature, cloud structure, and dynamics of venus middle atmosphere by infrared remote sensing from Pioneer Orbiter. *Science* 205, 65–67. Jul.
- Teanby, N.A., Bézard, B., Vinatier, S., Sylvestre, M., Nixon, C.A., Irwin, P.G.J., de Kok, R.J., Calcutt, S.B., Flasar, F.M., 2017. The formation and evolution of Titan's winter polar vortex. *Nat. Commun.* 8, 1586. Nov.
- Teanby, N.A., de Kok, R., Irwin, P.G.J., Osprey, S., Vinatier, S., Gierasch, P.J., Read, P.L., Flasar, F.M., Conrath, B.J., Achterberg, R.K., Bézard, B., Nixon, C.A., Calcutt, S.B., 2008. Titan's winter polar vortex structure revealed by chemical tracers. *J. Geophys. Res. (Planets)* 113, E12003. Dec.
- Teanby, N.A., Irwin, P.G.J., de Kok, R., 2010. Compositional evidence for Titan's stratospheric tilt. *Planet. Space Sci.* 58, 792–800. Apr.
- Teanby, N.A., Irwin, P.G.J., de Kok, R., Nixon, C.A., Coustenis, A., Bézard, B., Calcutt, S.B., Bowles, N.E., Flasar, F.M., Fletcher, L., Howett, C., Taylor, F.W., 2006. Latitudinal variations of HCN, HC<sub>3</sub>N, and C<sub>2</sub>N<sub>2</sub> in Titan's stratosphere derived from Cassini CIRS data. *Icarus* 181, 243–255. Mar.
- Teanby, N.A., Irwin, P.G.J., de Kok, R., Nixon, C.A., Coustenis, A., Royer, E., Calcutt, S.B., Bowles, N.E., Fletcher, L., Howett, C., Taylor, F.W., 2008. Global and temporal variations in hydrocarbons and nitriles in Titan's stratosphere for northern winter observed by Cassini/CIRS. *Icarus* 193, 595–611. Feb.
- Teanby, N.A., Irwin, P.G.J., Nixon, C.A., de Kok, R., Vinatier, S., Coustenis, A., Sefton-Nash, E., Calcutt, S.B., Flasar, F.M., 2012. Active upper-atmosphere chemistry and dynamics from polar circulation reversal on Titan. *Nature* 491, 732–735. Nov.
- Teanby, N.A., Sylvestre, M., Sharkey, J., Nixon, C.A., Vinatier, S., Irwin, P.G.J., 2019. Seasonal evolution of Titan's stratosphere during the Cassini Mission. *Geophys. Res. Lett.* (6), 3079–3089. Mar.
- Toigo, A.D., Waugh, D.W., Guzewich, S.D., 2017. What causes Mars' annular polar vortices? *Geophys. Res. Lett.* 44, 71–78.
- Tokano, T., 2010. Westward rotation of the atmospheric angular momentum vector of Titan by thermal tides. *Planet. Space Sci.* 58, 814–829. Apr.
- Vinatier, S., Bézard, B., Lebonnois, S., Teanby, N.A., Achterberg, R.K., Gorius, N., Mamoutkine, A., Guandique, E., Jolly, A., Jennings, D.E., Flasar, F.M., 2015. Seasonal variations in Titan's middle atmosphere during the northern spring derived from Cassini/CIRS observations. *Icarus* 250, 95–115. Apr.
- Vinatier, S., Bézard, B., Nixon, C.A., Mamoutkine, A., Carlson, R.C., Jennings, D.E., Guandique, E.A., Teanby, N.A., Bjoraker, G.L., Michael Flasar, F., Kunde, V.G., 2010. Analysis of Cassini/CIRS limb spectra of Titan acquired during the nominal mission. I. Hydrocarbons, nitriles and CO<sub>2</sub> vertical mixing ratio profiles. *Icarus* 205, 559–570. Feb.
- Vuitton, V., Yelle, R.V., Klippenstein, S.J., Hörst, S.M., Lavvas, P., 2019. Simulating the density of organic species in the atmosphere of Titan with a coupled ion-neutral photochemical model. *Icarus* 324, 120–197. May.
- Waugh, D.W., Randel, W.J., 1999. Climatology of arctic and antarctic polar vortices using elliptical diagnostics. *J. Atmos. Sci.* 56, 1594–1613.
- Waugh, D.W., Toigo, A.D., Guzewich, S.D., Greybush, S.J., Wilson, R.J., Montabone, L., 2016. Martian polar vortices: comparison of reanalyses. *J. Geophys. Res. (Planets)* 121, 1770–1785. Sep.
- West, R.A., Del Genio, A.D., Barbara, J.M., Toledo, D., Lavvas, P., Rannou, P., Turtle, E.P., Perry, J., 2016. Cassini Imaging Science Subsystem observations of Titan's south polar cloud. *Icarus* 270, 399–408. May.
- Wilson, E.H., Atreya, S.K., 2004. Current state of modeling the photochemistry of Titan's mutually dependent atmosphere and ionosphere. *J. Geophys. Res. (Planets)* 109, E06002. Jun.
- Yamamoto, M., Takahashi, M., 2015. Dynamics of polar vortices at cloud top and base on Venus inferred from a general circulation model: case of a strong diurnal thermal tide. *Planet. Space Sci.* 113, 109–119. Aug.
- Zuber, M.T., Smith, D.E., Solomon, S.C., Muhleman, D.O., Head, J.W., Garvin, J.B., Abshire, J.B., Bufton, J.L., 1992. The Mars observer laser altimeter investigation. *J. Geophys. Res.* 97, 7781–7797. May.